Air pockets and secondary habits in ice from lateral-type growth

Jon Nelson[1], Brian Swanson[2,3]

[1]Redmond Physical Sciences, Redmond, 98052, USA
[2]Earth and Space Sciences, University of Washington, Seattle, 98195, USA
5   [3]Laucks Foundation Research, Salt Spring Island BC, V8K2E5, Canada

Correspondence to: Jon Nelson (jontne@gmail.com)

Abstract. Often overlooked in studies of ice growth is how the crystal faces grow laterally. This paper explores the implications of such lateral-type growth and how it may explain air pockets and other secondary features of vapor-grown ice in air. For example, using a new crystal-growth chamber, we observed air pockets forming at crystal corners when a sublimated crystal is

10   regrown. This and other observations support the idea that the lateral spreading of a face, and its (in some cases) extension as a thin overhang over the adjoining region, is driven by a flux of surface-mobile admolecules across the face to the lateral-growth front. Inspired by recent work on this topic by Prof. A. Yamashita of Osaka Kyoiku University, we call this flux "adjoining surface transport" (AST) and the extension overgrowth "protruding growth", then apply the concepts to observed ice and snow crystals, including some from a cloud chamber and others from our experiments. We also suggest that such lateral-type growth

15   may explain other air pockets, droxtal centers in dendrites, hollow terracing and banding, multiple-capped columns, scrolls, trigonals, and sheath clusters. For dendrites and sheaths, AST may increase their maximum dimensions and round their tips.

1 Introduction

1.1 Normal growth, primary vs secondary habits, and interior features

Research on ice-crystal growth from the vapor usually focuses on the rates and mechanism of growth normal to the basal and

20   prism faces (e.g., Takahashi et al. 1991). The rates are sometimes called the linear growth rates, but to help distinguish normal from lateral growth, we use the other common term, the normal growth rates. These rates determine the crystal's maximum dimensions and aspect ratio, thus defining the primary habit. But ice and snow crystals usually have more complex shape features, such as hollows and branches, known as the secondary habit (e.g., Kikuchi et al., 2013). These features have recently attracted attention because the crystal "complexity" affects radiative scattering of ice-containing clouds (e.g., Smith et al., 2015;

25   Järvinen et al., 2018).

Secondary-habit features have also been observed for a long time. Wilson Bentley, known for his extensive photo-micrography work, paid much attention to the crystals' interior markings including various air enclosures (Bentley, 1901, 1924). For example, in his 1901 paper, he suggested that these markings and air pockets (enclosures) give clues about the crystal's trajectory, an idea no doubt true (yet unexploited). Later, Maeno and Kuroiwa (1966) examined the patterns of apparent air

30   enclosures in snow crystals, verifying through sublimation and melting that they were indeed enclosed pockets of air and not surface features. Much later, Yamashita categorized 16 types of pockets in tabular crystals (2016). Studies of other interior markings include those of hollows (Mason et al., 1963) and of ridges and ribs on branch backsides (Nelson, 2005; Yamashita, 2013; Shimada and Ohtake, 2016, 2018).

Although normal-growth processes, including the various growth mechanisms, provide a solid framework for understanding

35   the primary habit and some other crystal features, several common secondary habits remain inexplicable. These puzzling habits include i) the droxtal center seen in many dendritic snow crystals, ii) the thin basal planes in capped and multiple-capped

columns, iii) the abrupt bending of thin prism planes in scroll crystals, iv) the structure of sheath clusters, and v) trigonal crystals. Could lateral processes help explain these forms? We argue here that they can explain these and other complex ice-crystal features.

1.2 Concepts of lateral-type growth

5   In general, lateral growth is the increase in area of a crystal face. Thus, lateral growth trivially occurs when an adjoining facet advances normally, such as through direct vapor deposition. But lateral growth can also occur when there is no adjoining facet. We focus here on this latter, more interesting, case. Specifically, we assume the growth front for this lateral growth is a relatively small adjoining area at the face perimeter.

To help define our terms, consider the sketches in Fig. 1. Here, an initial droxtal with basal face b on top and prism face p in
10   profile undergo lateral growth in filling out the facets. Vapor flux to the basal face deposits water molecules that migrate over the edge e of the face, attaching at the smaller adjoining region between e and inside corner c, the lateral growth front. As shown later, this flux, hereafter the adjoining surface transport or AST, produces most of the molecular flux driving lateral growth L. In addition, vapor flux to the rough, curved region between faces produces normal growth N there, with the result that the spherical droxtal transforms into a solid hexagonal prism in (c). (During this process, b and p may be growing normally as well as
15   laterally; moreover, direct vapor flux to region e–c will also contribute to the lateral growth rate, but these aspects are not our focus.) After the prism fills out in (c), lateral growth as defined here ceases, and the normal growth proceeds alone.
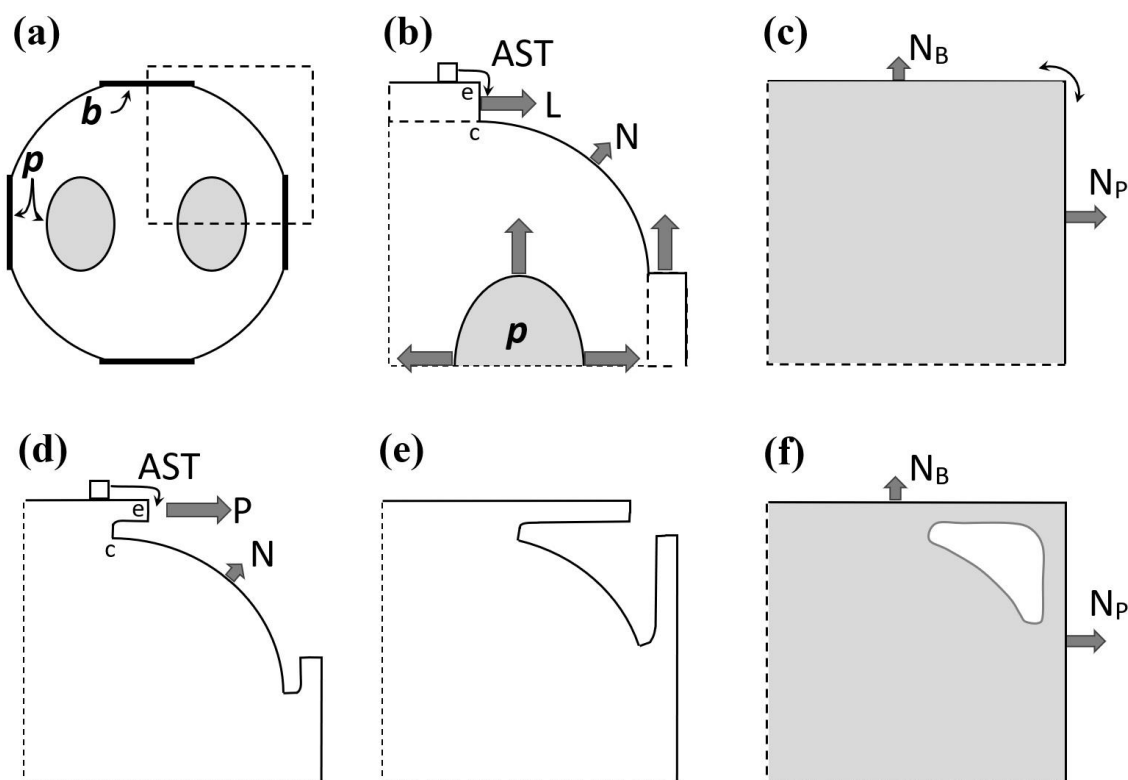
Figure 1: Concepts of lateral-type growth, droxtal-to-prism transition. (a) Droxtal front view showing small basal **b** and prism **p** faces. (b) Upper-right quadrant of (a), front view. Lateral growth **L** on top basal and right-side prism largely driven by adjoining surface transport AST. Normal growth **N** occurs on rough regions between faces. (c) Filled-out basal and prism faces. AST continues, likely with net amount to faster-growing face. (d) Different case following (a), instead having protruding growth **P**, also driven by AST. View is cross-section. (e) Continued protruding growth. (f) Filled-out basal and prism except air enclosure.

But in some cases, the AST flux plus the direct vapor flux does not completely fill out region **e**–**c**, and so the face extends as a thin planar overhang as shown in (d). Following Yamashita (2014), we call the growth of this planar overhang "protruding growth". With protruding growth **P**, the prism may incompletely fill out following the sequence (a), (d)–(f). The result of this protruding growth is an air inclusion, or pocket. The AST likely continues after the facets fill out, with the net flux possibly going in either direction as sketched in (c).

The evidence for AST on ice is indirect, partly coming from early studies of spreading ice layers on covellite (Hallett, 1961; Mason et al., 1963, Kobayashi, 1967). In these studies, the rates of approaching layers (micron-scale) changed in a way consistent with a flux of molecules over the top edge of the layer. The concept has long been applied to the growth rates of metal whiskers (e.g., Sears, 1955; Avramov, 2007), but rarely applied to ice. More recent experiments on ice find evidence for the flux over the tops of much thinner layers (Asakawa et al. 2014). For applications, earlier studies applied the concept of AST to the primary-habit change (Mason et al., 1963), but the specific mechanism has been criticized because it does not consider the role of critical supersaturation on the nucleation of new layers. Frank (1982) argued instead that AST should make the change of primary-habit with temperature more abrupt due to layer nucleation on one face hindering nucleation on the adjoining face. Yamashita (2015) has revived the general concept, expanding its applications, applying it to lateral and protruding growth.

This paper arose from two studies. In the first study, one of us (JN) had been examining images from earlier cloud-chamber experiments and images of precipitated snow with Prof. A. Yamashita of Osaka Kyoiku University, hereafter AY, exploring ideas about how AST may help explain some perplexing ice-crystal growth forms including pockets. Then, in a later study, we began measuring normal growth rates in a newly developed chamber, but unexpectedly discovered corner pockets appearing on a thick plate after a brief sublimation period. Recognizing the connection to the first study, we ran similar experiments, finding them to be reproducible and also revealing other types of pockets. We present our evidence and ideas here, with the goal of making a convincing case that such lateral-growth processes should be included in any complete ice-crystal growth model, particularly when modeling the more complex crystal features.

2 Observation methods

For this work, we used a new crystal-growth apparatus, hereafter CC2, that improves upon the capillary method in Nelson and Knight (1996). Like that apparatus, the observed crystal hangs pendant on an ultra-thin glass capillary within an isothermal, stagnant atmosphere. But in CC2, the ambient supersaturation around the crystal is controlled by the surface temperature of one of two vapor-sources in its own adjoining chamber, the connection of which is controlled by a translatable valve stopper. With this system, we can grow and then sublimate a given crystal without changing the temperature surrounding the crystal. The temperatures of the vapor-source surfaces are controlled by a thermoelectric element below each vapor-source container. The block encasing all three chambers is made of gold-plated, high-conductivity Te-Cu of dimensions 3" x 5" x 7" and submerged in optically clear cooling fluid pumped with a Neslab ULT-80 circulating cooler. To start an experiment, we insert HPLC water into the vapor-source containers and the capillary. The source water and capillary are cooled to the desired temperature and frozen. We then monitor the crystal at the capillary tip using back illumination and a full-frame DLSR 24-megapixel tele-microscope-camera system in the front. For more details of this apparatus and method, see Swanson and Nelson (2019).

We report here images collected from CC2 during their growth as well as images of crystals collected post-growth in sub-zero silicone oil by AY. The latter crystals were nucleated at the top of a tall (15-m) cloud chamber (Yamashita, 1971), and fell while growing for about 3–4 minutes under relatively uniform conditions. Although they provide only a snapshot of a crystal's growth, the high-magnification imaging provides greater detail of the early growth stages as well as growth at higher supersaturations,

5   thus complementing our CC2 results. Other crystal images were provided by Mark Cassino and Martin Schnaiter.

3 Observations and analyses

The following is more a survey of topics than detailed analyses of a given crystal feature. As such, most subsections largely stand alone with few references to others. Observations of lateral growth and various air pockets comprise most of the first 10 subsections. Specific habits are examined in §3.12, 3.14, 3.16–3.19, and 3.21. Lateral-growth theory is in §3.15 and the

10   appendices.

3.1 Lateral growth and corner pockets in droxtals

Large droxtals grown by AY in the cloud chamber show some aspects of lateral growth similar to the sketches in Fig. 1. For example, the droxtals in the top row of Fig. 2 show partially filled-out basal and prism faces, but with (a)–(c) also showing small circular pyramidal facets (not shown in Fig. 1). As the prism faces fill-out, they remain nearly circular to about one-half their

15   filled-out width, after which they become rectangular and fill-out before the basal faces fill-out, as in (d). The bottom row shows cases later in the crystal fill-out process. For example, (e) shows a filled-out prism with pockets in each corner, hereafter "corner pockets". Panels (f)–(h) show more complex growth, with (f) showing corner pockets, but also structures on the basal and prism faces. The prisms seem hollowed, but the top basal instead appears raised up. In (g), we see pockets where pyramidal faces would have been, suggesting pyramidal hollowing followed by protruding growth of the prism faces. Overhangs can be seen

20   where the corner pockets should appear. In (h), some normal growth has occurred after corner pockets formed, and this droxtal also appears to have pyramidal pockets as well as prism hollows.
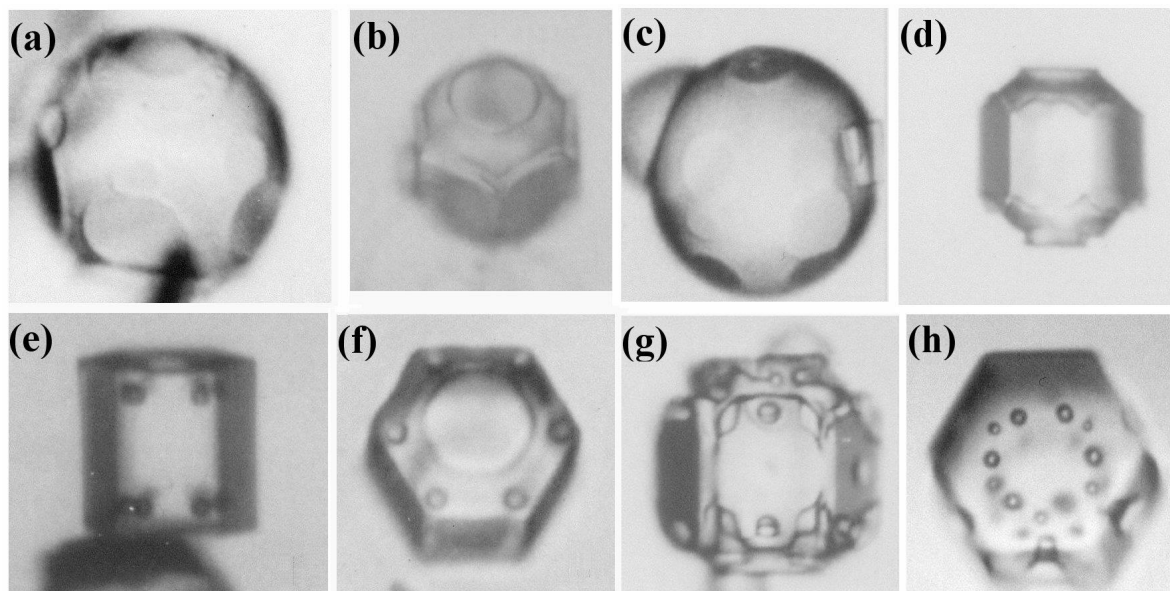
Atmospheric
Chemistry
and Physics
Discussions

Figure 2: Transitions between large droxtals and prisms at temperatures between −6 and −12 °C. Top row shows laterally growing basal and prism faces, with some pyramidal faces in (a) and (c). Bottom row shows filled-out faces with corner pockets in (e) and (f). (g) and (h) are more complex cases, but appear to show pockets where pyramidal faces hollowed, then were later overtaken by the prism faces. Sizes are within 45–90 μm. (From the cloud chamber.)

5

The size of the droxtals may be important for the formation of these corner and pyramidal pockets. In the cases shown here, the radii are all above 22 μm. In the figures of Gonda and Yamazaki (1978, 1984), the droxtals have radii of about 10 and 15 μm, yet do not reveal any pockets upon filling out. Their study examined droxtals at −7 and −15 °C with air present and supersaturations from 1–2% (1984 study) to water saturation (1978 study).

10   **3.2 Corner pockets on larger crystals during growth−sublimation cycle**

In our CC2 experiments, we observed the appearance of 12 small pockets, one in each corner, after a thick prism crystal resumed growth after a period of sublimation. The crystal, shown in Fig. 3, remained at −29 °C with a supersaturation that began at about 0.5%, then spent less than an hour at a small negative value, then went back to about 0.5%.
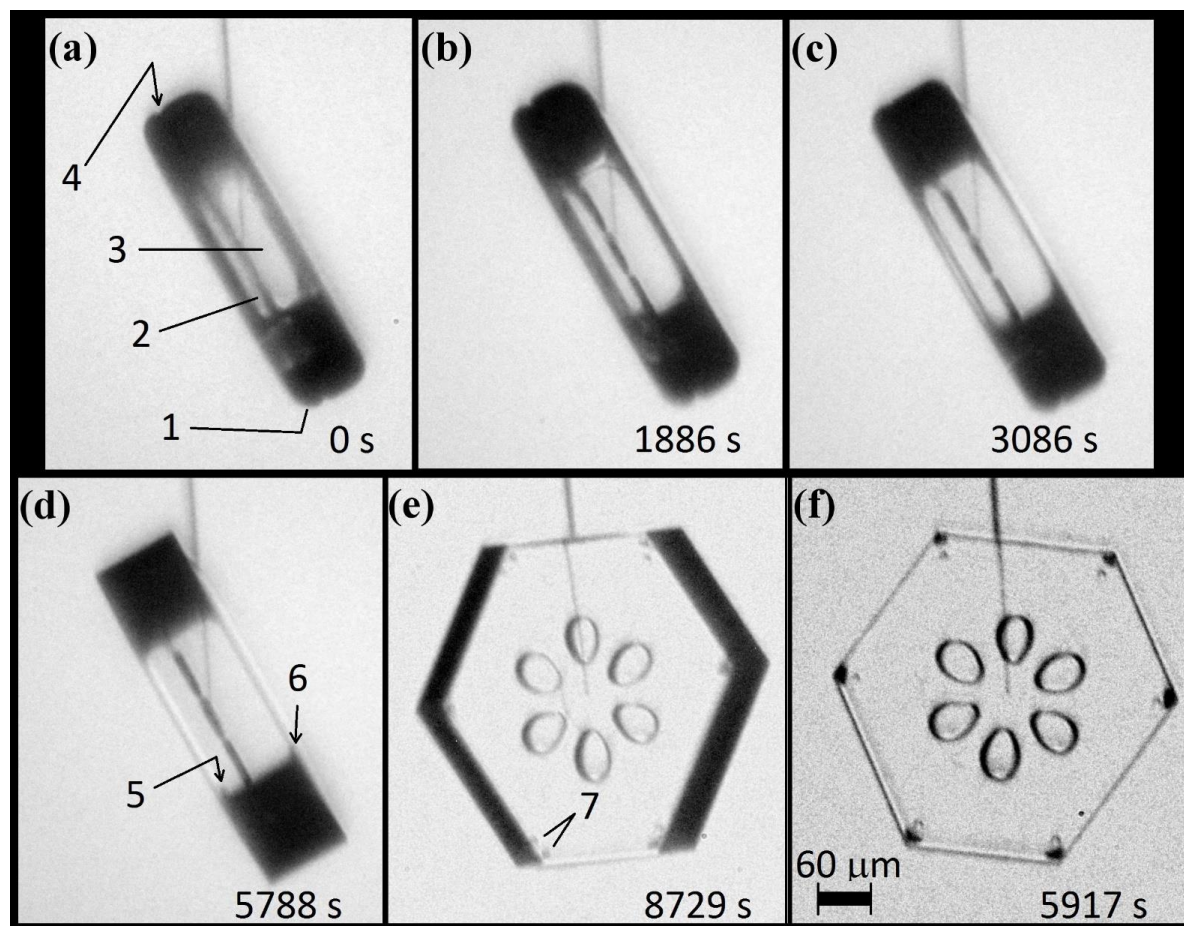
15   **Figure 3**: Corner-pocket formation at −29 °C after sublimation rounding. (a) Side-view of crystal at end of sublimation run. Marked point 1 shows a rounded basal-prism corner; 2, side view of interior planar air pockets; 3, view through two prism faces showing curved bounding edges (evidence from lack of sharpness); and 4, a perimeter groove bounding the same interior basal

plane as the interior air pockets. (b)—(e) Subsequent sharpening of the basal-prism corner under growth conditions. Marked points 5 and 6 appear to show side views of the corner pockets. (e) The basal face partly turned into view, showing a corner-pocket pair near each prism–prism edge at 7. (f) Front view showing the 12 corner pockets (two pockets per prism-prism edge, each pocket near opposing basal faces). Line coming down from the top is the capillary, terminating in the crystal at the nucleation point.

Consider the sequence in more detail. Figure 3a begins after the sublimation, just as the growth condition has returned. The lack of sharpness viewed through opposite prism faces in (a) shows that the faces retain some curvature. At the edge, the rounding appears to have a radius of about 30 μm. As time elapses in (b)–(d), the boundaries sharpen, becoming fully facetted in (e) and showing six pairs of pockets near the corners in (f). The slightly rotated view in (e) shows that each pair consists of one pocket near each basal face (top and bottom), and these pockets may be barely discerned even in (d) at "5" and "6". This particular cycle is the second one we imposed on this crystal, but it shows the corner pockets more clearly than the first growth-sublimation sequence on the same crystal.

The corner pockets in this case occurred on a tabular crystal, but the tabular shape is not crucial to the pocket formation. In another case, we had 10 crystals of various aspect ratios, including a long column, on three capillaries all undergo a growth–sublimation–growth cycle, and all exhibited the corner pockets. (Crystals in this case formed at higher temperature via a bionucleant and a method that allows several per capillary.) For example, Fig. 12b,d shows two cases on nearly isometric crystals. All of the cases though were on large crystals (~200–400 μm) at a temperature near −29 °C. In previous experiments (Nelson and Knight, 1998), we grew, sublimated, then grew crystals that were about 10x smaller (~15–40 μm) and at temperatures above −15 °C, yet never observed corner pockets. The literature shows other cases that were not recognized. For example, similar corner pockets appear on a ~100 μm crystal studied by Kobayashi and Ohtake (1974) above −20 °C after a sublimation cycle. In that case, the radius of curvature at the corner was about 20 μm, but they show another case without corner pockets in which the corner radius was only about 10 μm. Also, Magono and Lee (1966) show a solid, thick plate (photo #30) with corner pockets. In this case, the crystal was about 150 μm across with a curvature at the corner near 20 μm adjacent to the upper basal. Near the lower basal, the curvature appeared a little smaller and the corner pockets were smaller. Thus, although the phenomenon can appear on a range of crystal shapes, it may require that the corner radius exceed a certain value. At about one atmosphere pressure and temperatures near −20 and −30 °C, this critical radius may be between 10 and 20 μm, but the value may depend on temperature and pressure.

3.3 Planar pockets formed under constant conditions

Six thin, petal-shaped pockets also formed on the crystal in Fig. 3. These appeared well before the formation of the corner pockets, and did not require a sublimation event before formation. From the front (f), they appear typical of common center hollows (i.e., formed in face centers) that later closed up, but the side view (d) shows them to be unusually thin. Hence, we call them planar pockets. In (a), the planar pockets appear to be in the same plane as the small notch marked "4". The notching suggests a disordered region, like the eroded region at the grain boundary near the center of bullet rosettes. However, the prism planes align on both sides of the notch, showing both sides have the same crystal orientation. Thus, the notch and plane must have a stacking fault, not a grain boundary, with the depth of the pockets suggesting that a region of faults may be present. Itoo (1953) called such crystals "twin prisms", and found them to be very common in a light precipitation at −30 °C. Kobayashi and Ohtake (1974) made a similar observation to that here, suggesting a specific type of stacking fault. A more recent study found that extended regions of stacking disorder are common when small water droplets freeze near −40 °C (Malkin et al. 2012), but are unlikely to form during vapor growth (Hudait and Molinero, 2016). The crystal of Fig. 3 began with a freezing event at the

Atmospheric
Chemistry
and Physics
Discussions

tip of the capillary, where the apparent stacking-disorder region intercepts, but grew from the vapor. Thus, the argument for the source of the notch and planar pockets is consistent with these recent studies.

Another distinctive feature of these pockets is their near-perfect six-fold symmetry. Such symmetry of both the pockets and the crystal is unusual for a crystal grown at such low supersaturation. A reason for their symmetry is given in §3.11.

5 **3.4 Lateral growth of the basal face**

In some crystals, we can observe the spreading of the basal facet when the partly sublimated crystal begins to grow. For example, the sequence in Fig. 4a–e shows an expanding ring on the basal face. When this ring reaches the perimeter, the crystal appears fully facetted and the corner pockets appear (arrows in (e)). Thus, the rings mark the expanding boundary of the basal face (as opposed to a macro-step on a growing face). The positions of these rings are marked in (f), with the time interval (units of 5 min)

10 between marked positions in the upper right. The markings show a significant slowdown as the facet perimeter approaches the crystal perimeter, and in this process, the facet perimeter becomes more distinct. The latter observation is consistent with a thicker height difference between the rounded surface and the facet upon reaching the perimeter, consistent with a rounded edge, and lateral growth driven by AST.
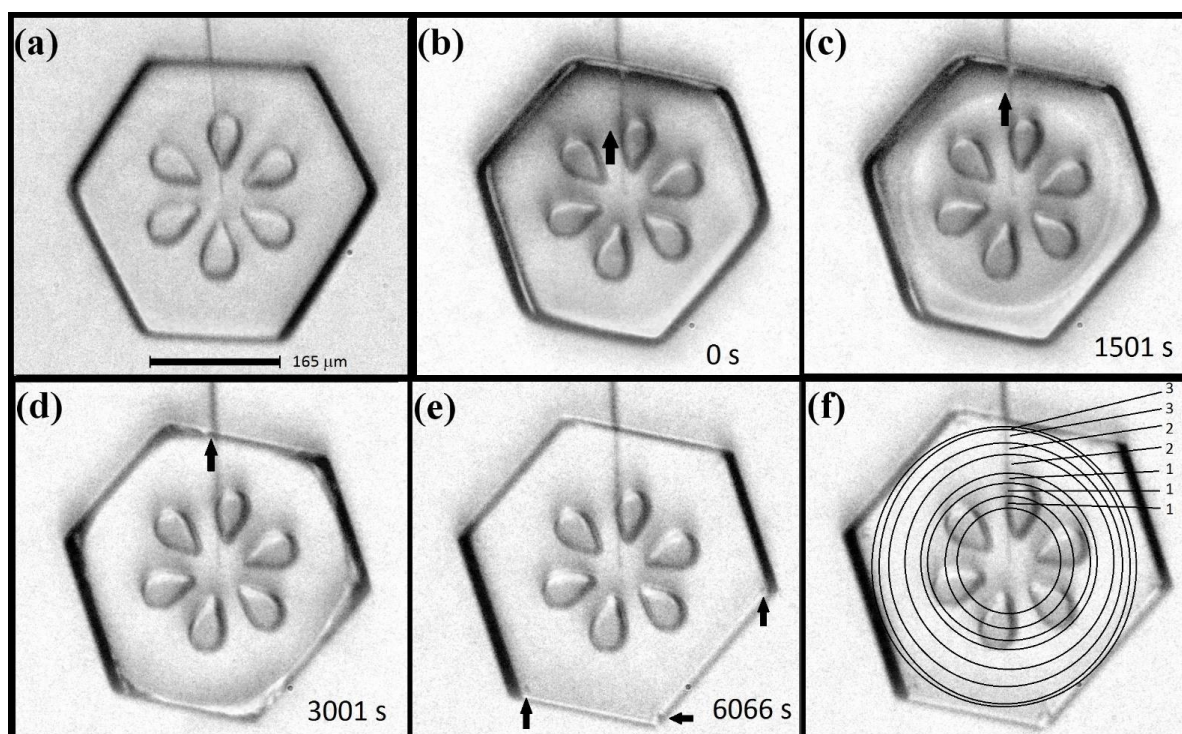

15

Figure 4: Expanding basal facet with corner pocket formation. (a) Crystal just before sublimation. (b)—(e) Same crystal, during a second growth period, just after the sublimation period. The thick arrow marks a barely visible boundary of the basal facet, roughly forming a circle. In (c), two such circles can be seen, representing the boundaries on both basal facets. The times of the images are in their bottom right corner. In (e), the arrows mark the corner pockets. (f) Same image as (e), but with the estimated
20 basal perimeters sketched with circles. Numbers at right are the times between the perimeter sketches in units of 5 minutes. Data is plotted in Fig. 5.

To test the AST-driven lateral-growth explanation, we ran several calculations involving three models for the lateral growth. The first (I) is normal growth of the lateral-growth front (i.e., **e–c** in Fig. 1b) driven by direct vapor flux. In this case, the lowest curve in Fig. 5 shows the resulting advance to be about two-orders of magnitude too slow. Also, the trend, which is seen more clearly with an assumed 40% supersaturation, does not capture the slowdown that begins within about 1000 s of the start. Case II

5 is the AST-driven case, and this fits the data well provided that the calculation uses the inset trend of h/x_s (normalized height of lateral-growth front). This profile of the growth-front height h is difficult to compare to the crystal, as it requires frequent side views of the crystal that we did not obtain, but it is a reasonable fit to the initial side view. Case III is an approximate rate based on normal growth of the rough region beyond the lateral-growth front. It does not fit the data well, but is better than case I. Also, case III is sensitive to the profile of the rough region. Thus, the failure to fit the curve may be due to profile inaccuracy.

10 Appendix A has details of all three model calculations. A better test of the lateral-growth mechanism requires better data, such as interferometry data (e.g., Shimada and Ohtake, 2016) and possibly a model that includes both mechanisms II and III.
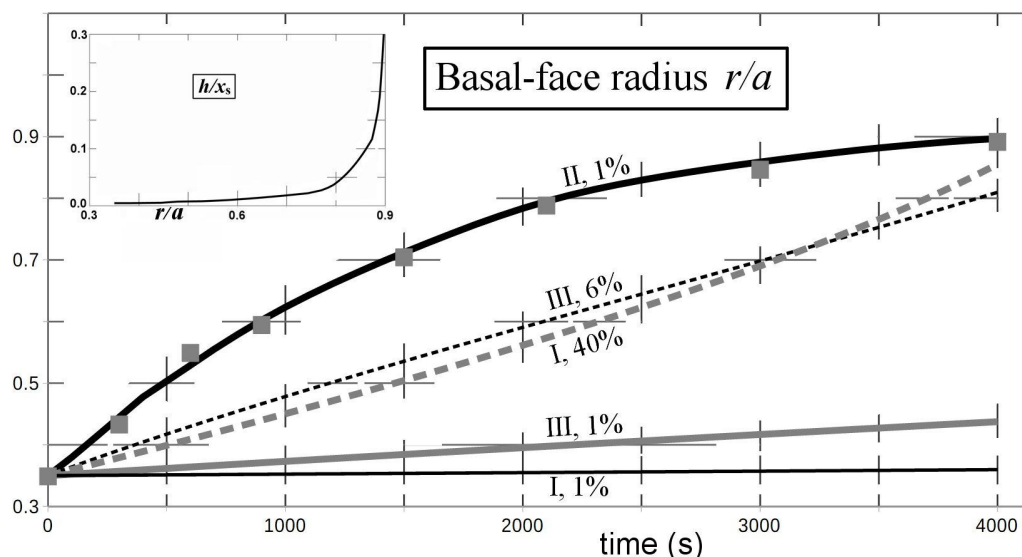

Figure 5: Lateral growth of basal from Fig. 4 (solid squares) with model fits I–III from Appendix A (curves). (I): normal growth
15 of the facet edge. (II): the lateral growth of the facet edge from AST. (III): and the normal growth of the rough, rounded region. Curves are also marked with the assumed supersaturation. Calculation details are in Appendix A. The radius a is the mean value out to the prism–prism edge. Hatch marks are truncated gridlines. Inset plot shows values of facet-edge height h used in the fit for case II, x_s is the surface migration distance.

20 Nevertheless, the observed behavior is consistent with growth being driven by a flux of surface mobile molecules, the AST mechanism, from the facet to the lateral-growth front. Also, one can see that the prism–prism edges appear to sharpen by (d), before the basal face fully spreads out. We can see similar behavior in our next case.

Atmospheric
Chemistry
and Physics
Discussions

Open Access

3.5 Corner pockets on a non-symmetric thick plate and on naturally formed crystals

In another case, we ran a growth–sublimation–growth cycle on a tabular prism at −30 °C with unequal prism faces. In this case, shown in Fig. 6, the initial crystal in (b) is more rounded than that in the previous case, with a radius of ~30–40 μm. After regrowth (supersaturation below 1%), the facetted crystal emerged with larger corner pockets that are elongated along the edges 5 (e). And, as with the previous case, the spreading of the basal facet slows down upon nearing the edge in (b) to (d). Later in the growth, in (e), a large basal hollow appears. But the larger size of the corner pockets in this case compared to those in the cases in Figs. 3 and 4 is consistent with the pocket size being larger for cases with larger initial corner radii.
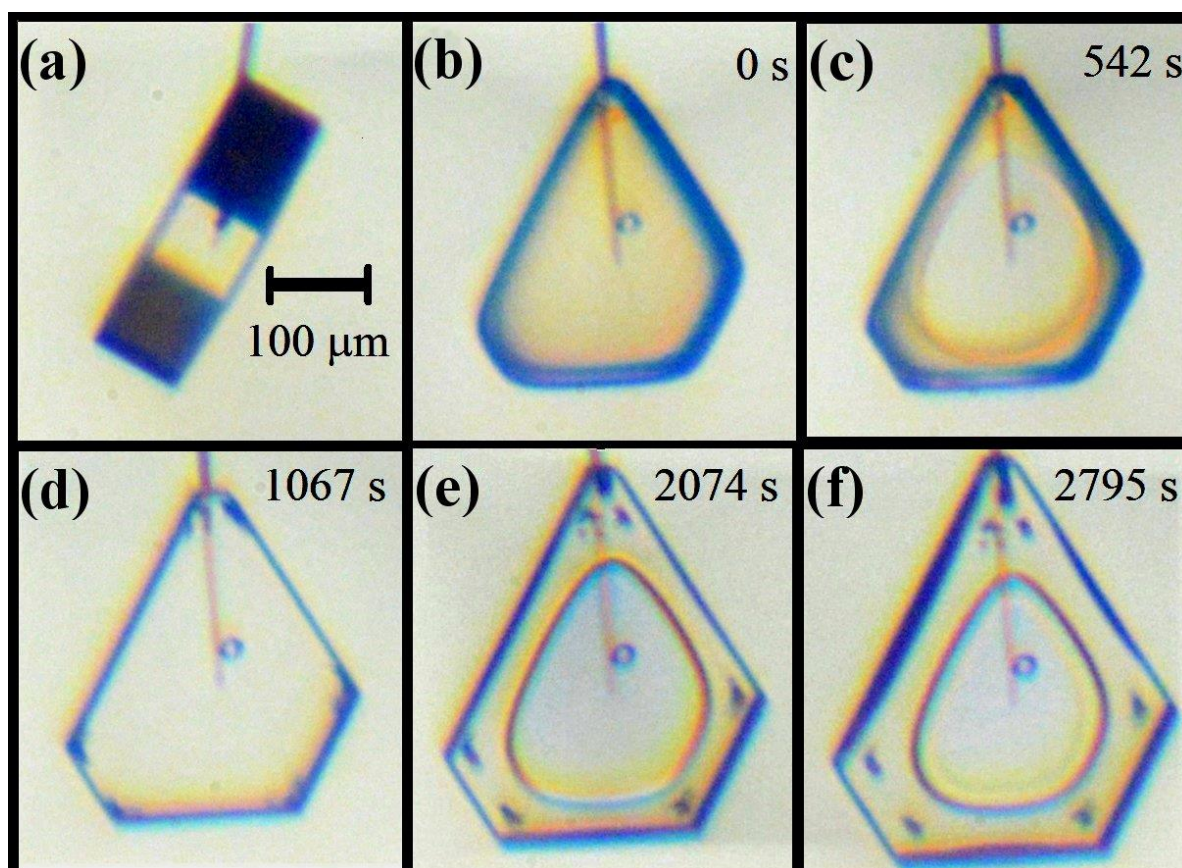

10 **Figure 6**: Corner-pocket and center hollow formation and changes on a non-symmetric crystal. (a) About 2 h before sublimation. (b) Immediately after sublimation, growth period starting. (c) Basal facet spreading. (d) Clear corner pockets formed. (e) After normal growth, a center hollow on one basal and on top prism. (f) Further growth, some hollowing starting on wider prism faces.

Corner pockets such as those described here also appear on natural snow and ice crystals. The center of the snow crystal in Fig. 15 7a, collected and photographed at the ground, shows pockets "CP" in the corners of the central plate. Case (b) shows apparent corner pockets in a thin, solid tabular prism collected in-cloud. In (c), we see six pocket pairs near the center of another collected snow crystal. This case is not as clear as that in (a) because they appear on a two-level crystal. We also show other pockets further up a main ridge in the smaller inset at bottom. Thus, these do not appear to be the same corner pockets that we have

discussed above. This type is discussed later, in §3.13. For the cases in (a) and (b), the crystals may have undergone a
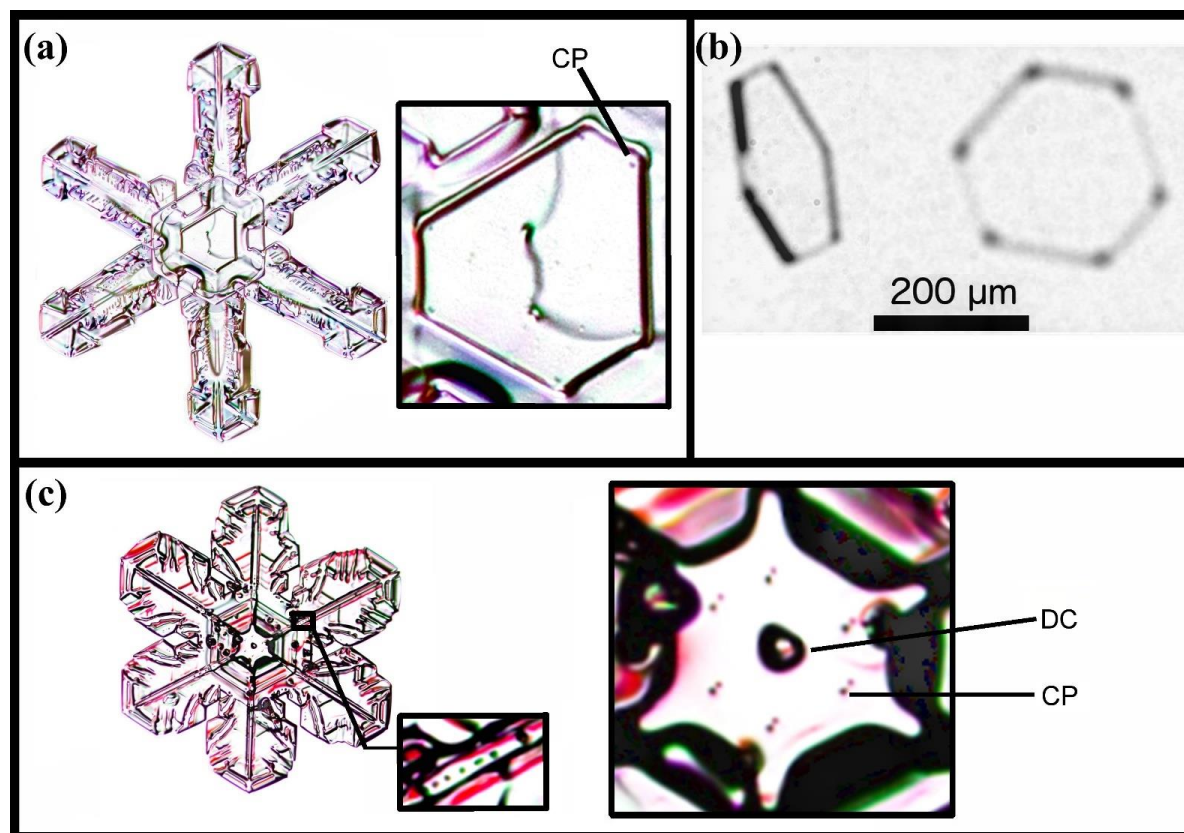sublimation period to produce the corner pockets.

5 **Figure 7:** Corner pockets (CP) and droxtal centers (DC) on natural snow and ice crystals. (a) A narrow broad-branch crystal.
(Curved line through crystal center is an imperfection on the glass slide.) (b) Crystal collected on the SOCRATES mission at -
24.9 °C, viewed at two angles. Image courtesy of Martin Schnaiter. (c) Case of a wide broad-branch, large inset at right showing
a close-up of center, small inset shows pockets along one ridge. Snow crystal images in (a), (c) courtesy of Mark Cassino.

10 **3.6 A basic mechanism of corner-pocket formation**

Existing views on normal growth via step motion cannot readily explain corner pockets. With normal growth, each pocket must
have at one time been a hollow (lacuna or concave feature) before closing-off to enclose the air. And standard hollowing theory
(e.g., Kuroda et al., 1977; Frank, 1982; Nelson and Baker, 1996) predicts that hollows form around a local vapor-density
minimum, not at a corner where the driving force for normal growth is instead a local maximum. We argue here that they form

15 via protruding growth, similar to that in Fig. 1d–f. But unlike the droxtal case, sublimation is needed here.

Consider the stages in Fig. 8, with an oblique view at left and a cross-section through a corner at right. In (a), the crystal is a
thick prism and fully facetted, representing a growth condition. In (b), the crystal has transitioned to a sublimation condition,
thus rounding its corners and edges. Then, in (c), a growth condition resumes, causing the basal and prism facets to grow
laterally, primarily via AST over the spreading edge-front where they bond. As the spreading edge becomes thicker (viewed in

20 cross-section), this rate will slow because the same number of molecules must spread over a wider front region. This growing

front becomes too wide in (d), and the AST flux of molecules builds up an overhang on the spreading facet edge, initiating protruding growth. Where the protrusions from two faces intercept, they merge, halting further protrusion there. This merging occurs first further back along the edge from the corner, but progresses to the corner at (e), sealing-off the corner pocket. Later, sublimation and deposition within the sealed-up pocket will round out its interior, making the pocket more spherical. This

5   mechanism does not include normal growth because normal growth in the experiment was extremely low.

The case in Fig. 3 shows six dark corner pockets on one basal, six lighter pockets slightly further inside (radially) on the other basal. This difference may have arisen from having different degrees of initial rounding, or by one basal face having more basal-normal growth than the other. The side views show how the planar pockets are closer to the left basal face, indicating both that the left-side rounding may have a smaller radius and also that the right basal face has a greater normal growth rate. Further

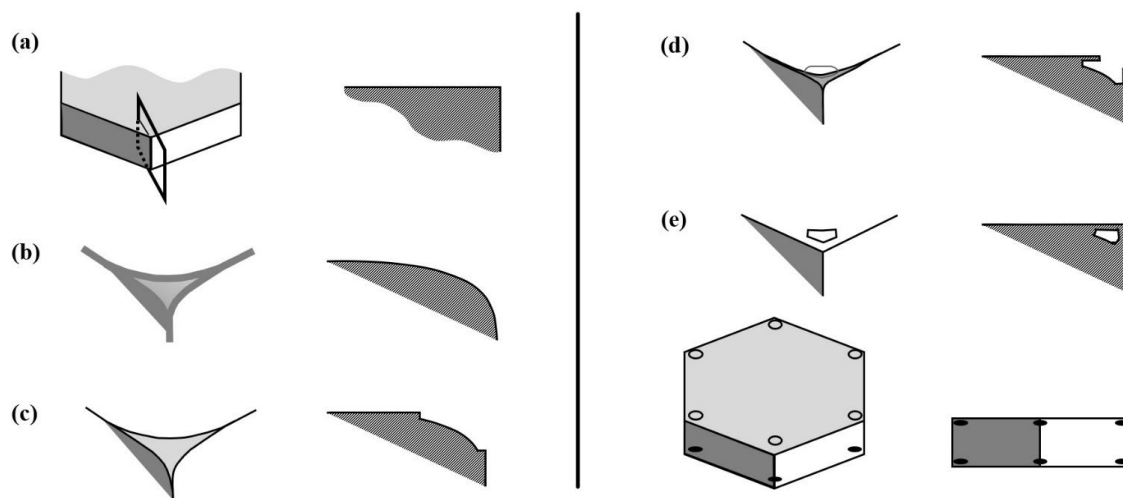10   considerations of how normal growth may affect pocket formation is in §3.8.

Figure 8: Corner-pocket formation after sublimation rounding. (a) Oblique (left) and cross-section (right) view of edge of a tabular crystal during growth. The top face is basal, the sides are prism. (b) Same views after net sublimation rounded the edge.
15   (c) After growth conditions resume. Basal and prism have facet-edge fronts (same as Fig. 1b). (d) Protruding growth begins. (e) Corner pocket forms. Overall oblique and front view at bottom.

3.7 Lateral growth on the prism faces and elongated edge pockets

The corner pockets can vary in size and shape, with those in Fig. 6 being larger and longer along the edge than those in Figs. 3
20   and 4. This elongation can extend along the edge, traversing nearly the entire edge. The example in Fig. 9 also involves a more complex crystal, with interior edges. It begins from a sublimated, rounded form at 0 s. After 180 s, small prism facets started to appear (not shown). These facets grow both normally and laterally as the other facets become defined. At 541 s, the edge at 'A', as well as the edges of face 1, extend slightly above the plane of the adjacent faces. By 1083 s, some normal growth can be discerned. From 1444 s, the two opposing edges of faces 2 and 3 become clear, and these edges approach each other at later
25   times, completely merging before 8448 s. Later, the final front and side view shows that this edge region has a long pocket along this prism–prism edge marked 'E'. Thus, the merging of two lateral-growth regions created an elongated edge pocket between

prism faces. As this is the only case we observed, we do not know if the complex nature of the crystal was essential or the greater amount of normal growth than those in the previous cases.
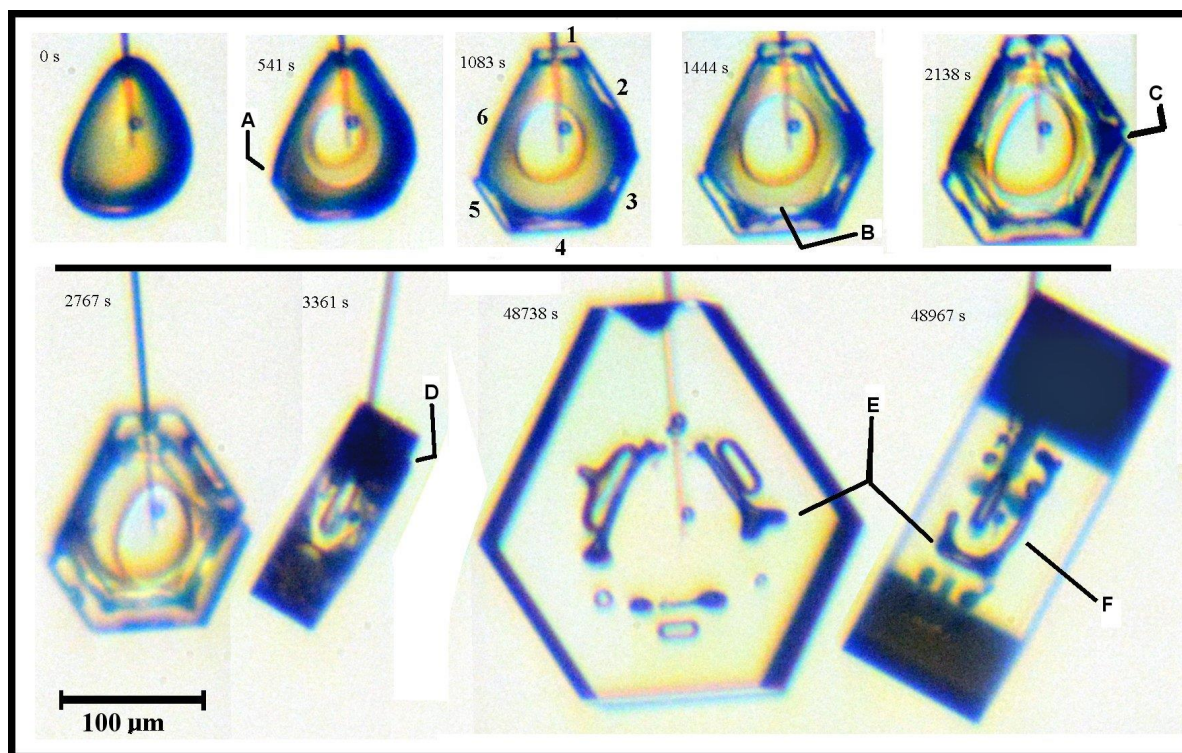

Figure 9: Elongated edge pockets and lateral face growth on a complex crystal growing under constant conditions. Time 0 s is just after sublimation, the crystal just starting to grow. At 541 s, **A** marks the edge of prism face 5, growing laterally over face 6. The prism faces are filled out by 1083 s and numbered clockwise from top. Face 5 growing laterally over face 6. The **B** at 1444 s shows a boundary with straight edge. **C** at 2138 s shows two adjacent prism faces closing up via lateral growth (completed before 8448 s, leaving an elongated edge pocket). At 3361 s, **D** marks an interior edge of a thick layer on the bottom basal face. **E** marks two views of an edge pocket between prism faces (same as that tracked by **C**). **F** is an elongated edge pocket between the bottom basal face and prism face 2.

Such merging of straight-edged sections may be occurring on the basal face as well. By 1444 s, dark regions appear along basal-prism edges, suggesting that the corners are connected by long pockets. Such an edge pocket is confirmed and marked 'F' in the final side view. However, unlike the prism–prism-edge case, the lateral growth involved in this feature's formation is unclear. The lateral spreading of a thick layer on the old basal face, with edge boundaries parallel to the basal-prism edge, may explain this edge pocket. Two indications that such a thick layer may have spread as such are marked as 'B' and 'D'.

The dendrite in Fig. 23c shows similar edge pockets at sidebranch D, but the formation conditions are likely different. The formation of elongated edge pockets in both cases likely require protruding growth even if the details of the mechanism differ.

3.8 Mechanism of edge, elongated-edge, and edge-pair pockets

The formation of edge and elongated-edge pockets should be similar to that of the corner pockets. For the elongated-edge pockets in Fig. 9, one difference from the corner pocket case is that the advancing front of the laterally growing facet is straight and parallel to the crystal edge. Another difference may be the higher normal-growth rate (though still quite low). These differences suggest the mechanisms in Fig. 10.
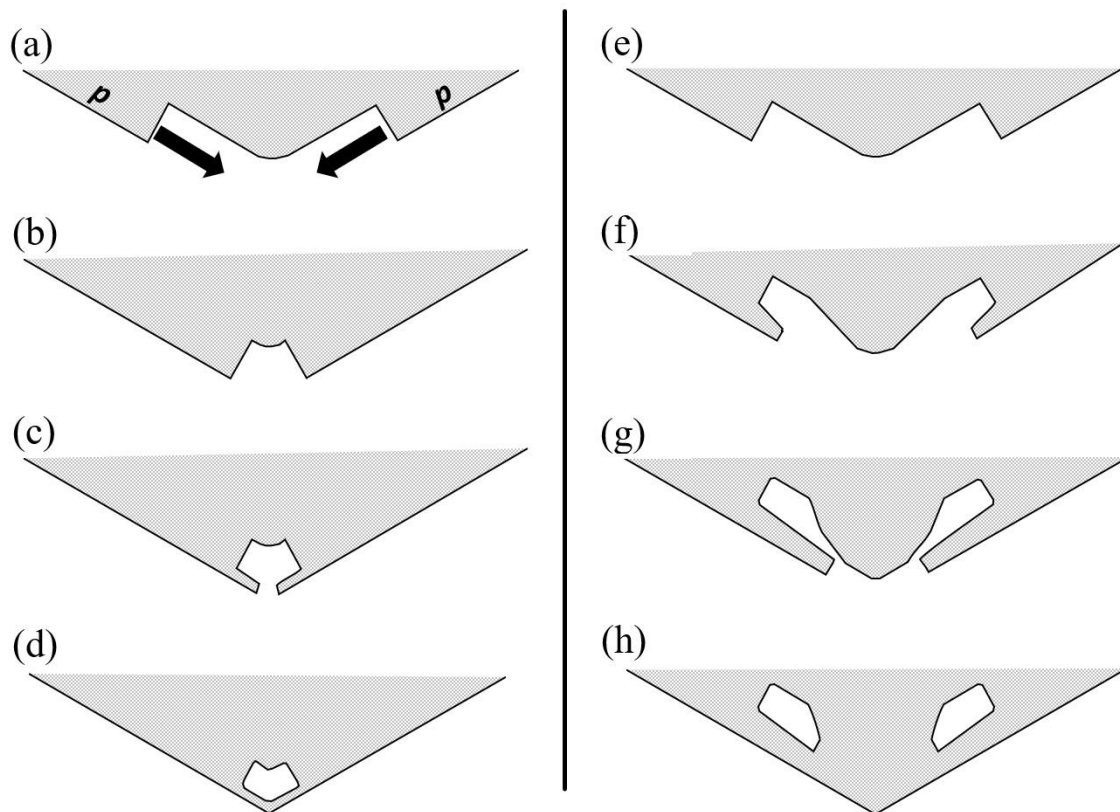
Figure 10: Edge-type pocket formation between prism faces. (a) Each prism face has a large advancing front or side-face growing laterally towards the edge. This lateral growth is marked by the solid arrows and is driven by both direct vapor flux and the AST flux. (b) The two large fronts are close enough to effectively 'shadow' the inside edge from the vapor flux. (c) Vapor gradients along front leads to protruding growth, driven by AST. (d) Protrusions merge, making an elongated edge pocket. Case (e)–(h) is similar except with greater normal growth. The two side fronts may also be non-crystallographic as in scallop-type rounded growth.

In (a), the two new prism facets converge on an existing prism–prism edge. Their advancing fronts may be prism faces (as in Fig. 9) or non-crystallographic. If the front is thin, then protrusive growth may occur only near the corner where the rounding is greater. So, we consider thicker fronts in this mechanism. The motion is driven largely by AST, but some direct vapor deposition to the front will contribute. But when the two fronts converge, the interior region would get increasingly shielded and shut out from vapor (b) at the same time that the front height starts to increase due to the rounding. Thus, the AST produces protrusions (c). Upon merging, they leave a pocket parallel to the edge (d). This pocket may be nearly equidimensional for the edge pocket, and elongated if the prism–prism edge is long. This enclosure would then be completely sealed up by lateral and protruding growth on the basal faces (not shown).

A pair of pockets may form near an edge or corner instead of one. Although all stages in this process have not been observed, Libbrecht (2003) shows a double-edge case in a thin plate grown at −15 °C, and Knight (2012, Fig. 3c) appears to show some that are more widely spaced at −5 °C. Bentley (1924) shows several cases (e.g., his figures 6, 32). Such cases may arise when even greater normal growth occurs with the protruding growth as sketched in Fig. 10e–h. Although the normal vapor flux may

compete with the AST flux, it may also create vapor-density gradients that can favor protrusion formation on one face versus another. For example, if the case in (e)–(h) represents a thin plate, the vapor-density gradients (discussed in §3.10) would favor initiation of protrusions on the prism faces as shown, but not necessarily from the AST flux from the basal. However, as argued in §3.16, the AST flux from the basal should be larger for points nearly $\sim x_s$ back from the tip. Thus, the AST flux from the basal

5   could produce protrusive growth away from the corner, but not at the exact corner. Thus, the corner can fill-out as shown due to both normal flux and AST flux from the basal. The result is a pair of pockets as shown in (h). This process requires that the initial stage (e) have a rounded prism–prism edge. Knight (2012) observed that the thin plates often began rounded, and scalloped, lacking any prims faces, and later became fully facetted plates (see §3.16 for similar cases). Thus, this mechanism does not require a period of sublimation rounding.

10   **3.9 Hollow close-off to center pockets and terracing**

Under a wide range of growth conditions, a center hollow may form on one or more crystal faces. Libbrecht (2005) and other authors (e.g., Gonda and Gomi, 1985) have referred to the process as an instability. In the standard treatment, however, the hollow occurs when normal growth of the entire facet becomes impossible (e.g., Kuroda et al., 1977; Frank, 1982). Impossibility or instability, which is it? The standard "impossibility" treatment seems qualitatively successful in some cases of middling

15   supersaturation (e.g., Nelson and Baker, 1996) and at relatively high supersaturation where the hollow tends to keep enlarging in width (e.g., hollow columns) or advance into branches (e.g., dendrites) in a generally consistent, repeatable fashion. But at low supersaturations, the hollow often varies in width, getting wider, then getting narrower, and finally closing-off into a center pocket. Oscillations also occur at middling-to-high supersaturations (e.g., Smith et al., 2015), but are much more pronounced at the low supersaturations in our experiments here. Gonda and Koike (1983) also observed the closing-off of hollows during

20   growth at one atmosphere and supersaturations up to 33% at −30 °C. At low supersaturations, otherwise identical faces can have different patterns of hollows and pockets. Thus, at least at low supersaturations, the hollow phenomenon does seem to have some qualities of an instability. We provide supporting evidence here, and suggest a basic instability for low growth rates in §3.10.

Both the width oscillations and closing-off behavior occur in the crystal of Fig. 11. In this case, hollows are just forming at 4419 s on the prism faces, as shown in (a), with wider hollows on the wider faces. But by 8210 s (b), different hollows have

25   changed differently. On prism face "1", as marked in (a), the hollow has remained small. On face "2", the hollow width suddenly increased at some time between 4419 and 8210 s, but is now decreasing in width (i.e., the rim is narrower than that just inside the rim). This sudden increase in hollow rim-size creates a flat terrace-like feature in the hollow, so we refer to this as hollow terracing. The initial formation of hollows on faces 2, 4, and 6 are also flat, consistent with their later terracing. On faces 3, 4, and 5, the hollows are gradually closing up, again, with the rim leading the way. Face 6 displays behavior like that of 2, except

30   the hollow widths are more clearly decreasing before abruptly increasing. In addition to these, a basal face has a wide hollow in its center that slightly decreases in width from (a) to (b). All these trends continue for at least another 8000 s in (c), with the bottom three prism faces (3, 4, 5) now completely sealed center pockets. The side view in (d) shows how just the basal face on the left (facing up) has hollowed, but has narrowed at the rim from (b) to (c).
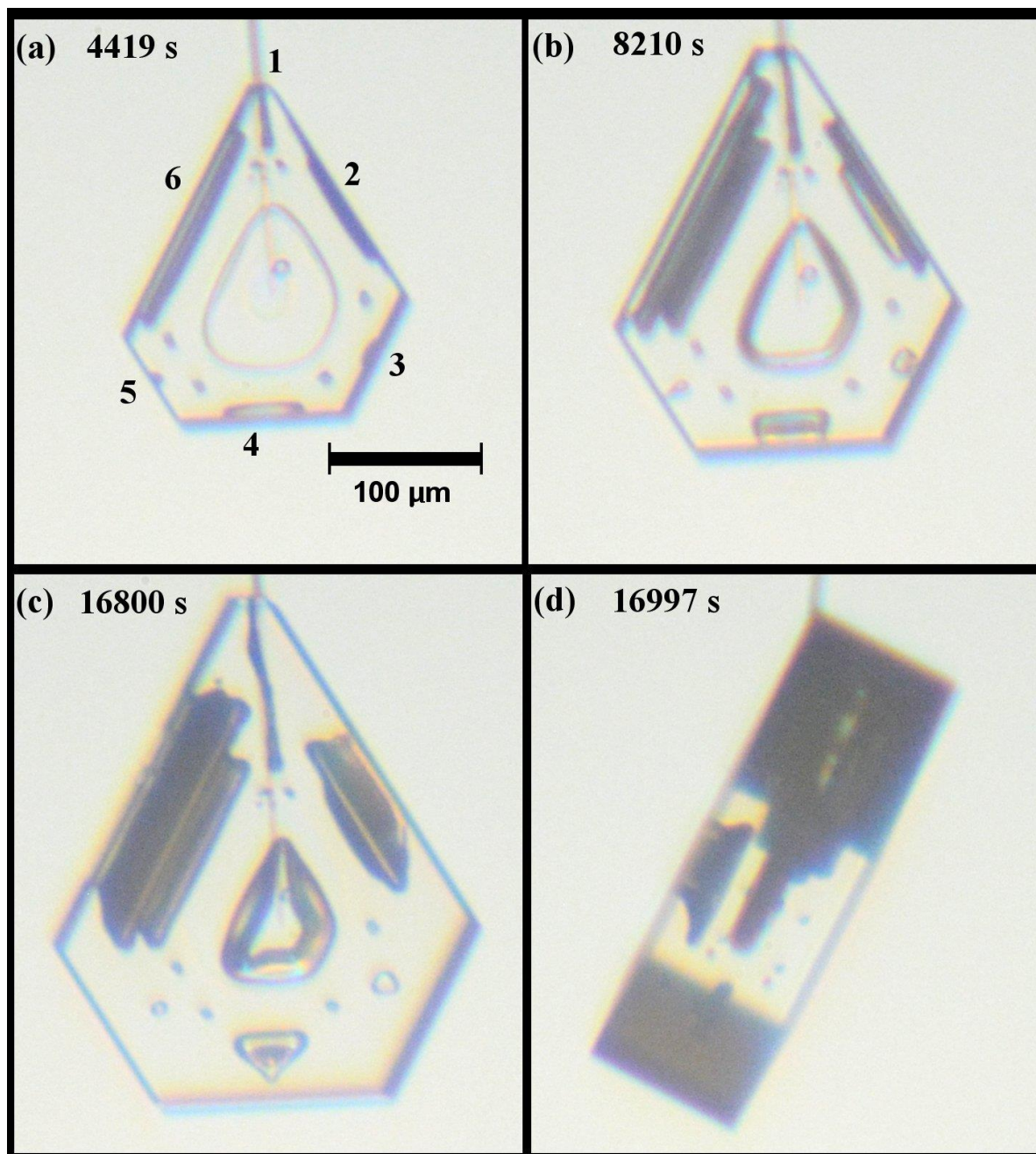
Atmospheric
Chemistry
and Physics
Discussions

Open Access

EGU

Figure 11: Center hollow development and center pocket formation. The crystal is the same as that in Fig. 6, but at later times. The scale in (a) applies to all images. Numbers in (a) label the six prism faces. Image (d) is a side view.

5   This oscillating-width nature of some of the prism hollows also occurs with basal hollows. In Fig. 12, we show two cases. In the top row, initially, in (a), the basal faces have hollows that 'fan open' at their start, that is, have an increasing width during growth, but then have nearly straight sides, indicating a constant rim diameter of the hollows. Soon thereafter, the hollow rim suddenly widens, forming a terrace feature in (b). A similar progression occurs in the crystal in the bottom row, with two such

terraces forming on the face on the right in (d). Except for a brief sublimation period (note the corner pockets), the growth conditions remained constant throughout the 47 hours of growth.
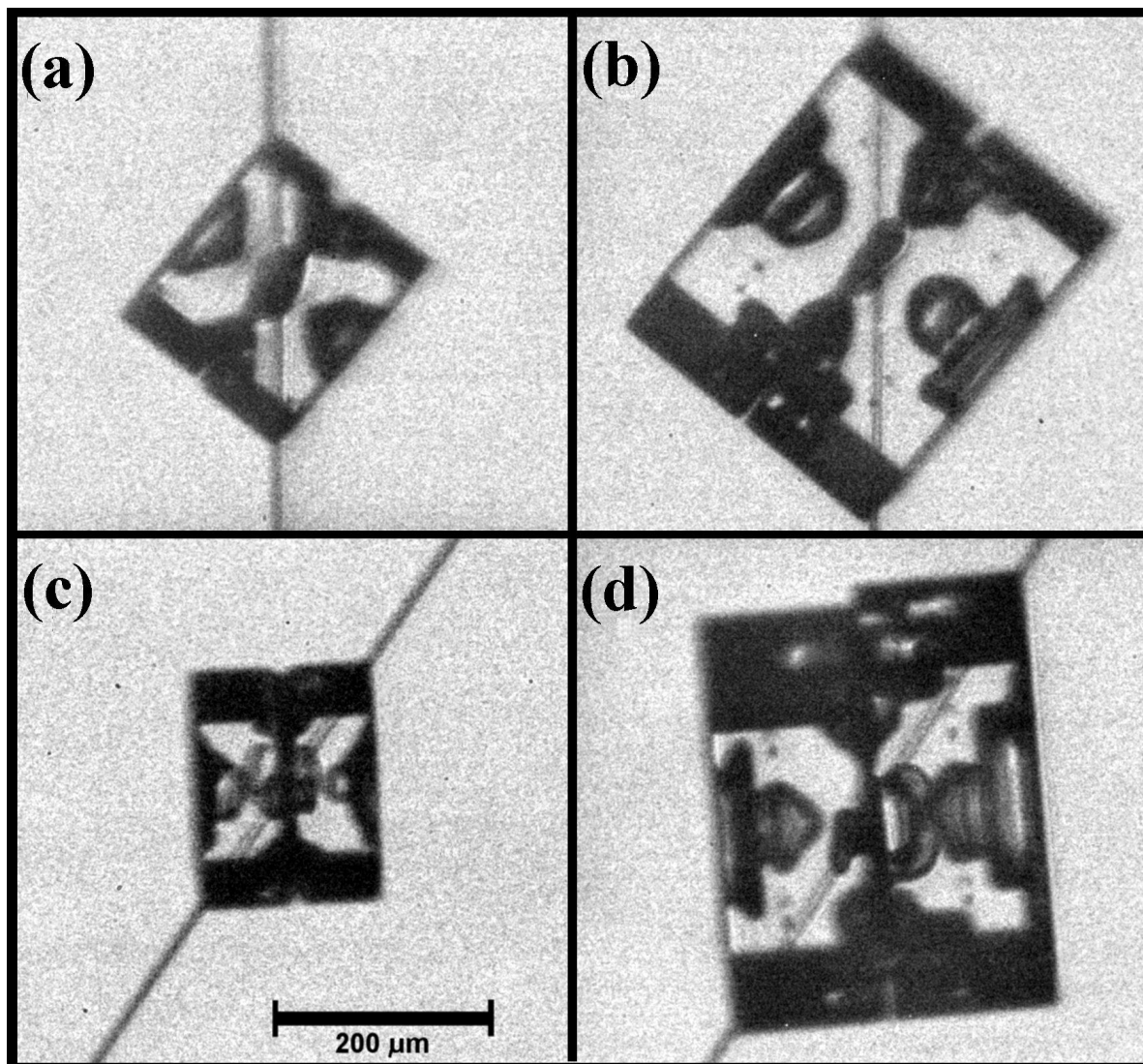
5 **Figure 12:** Center hollow terracing on twinned crystals grown under constant conditions. (a) Side view of crystal in middle of one capillary, basal faces pointing NW and SE. (b) Crystal in (a), but 46 hours later. (c) Different crystal under the same conditions, but on a different capillary. (d) Crystal in (c), but 47 hours later. Small corner pockets also appear in (b) and (d) due to a brief sublimation period after images in (a) and (c). Scale in (c) applies to all images.

10 **3.10 Mechanisms for hollow close-off, terracing, and banding**

The center hollows shown here exhibit variable behavior at low supersaturations, even under near-constant conditions. For example, the hollow's size and shape can vary considerably between different faces of the same crystal. Also, a given hollow's width can change suddenly, often showing periodic terrace-like features, and sometimes closing-off completely, leaving a center

Atmospheric
Chemistry
and Physics
Discussions

pocket. Such behavior suggests a complex process involving competing influences and a possible instability. Here we describe a simplified mechanism for such an instability between normal and protruding growth, and argue that the growth behavior of adjacent faces may influence hollows, particularly at low supersaturations, possibly leading to the above-mentioned observations.

5 The overall driver of hollowing of a surface is lateral supersaturation (σ) gradients across the surface. These gradients are influenced by growth on the crystal faces such that, for example, normal growth on the basal face produces a decrease in surface supersaturation, starting from a high value in the middle of the prisms p, as sketched in Fig. 13a, to the p–b edge, to the smallest value in the center of the basal. Normal growth only on an adjacent prism faces produces the opposite gradient on the basal (dotted lines). In general, normal growth occurs on all faces, and thus the contributions from both sets of contours in (a) are

10 added with a weight in proportion to the normal growth rates (Nelson and Baker, 1996). Concerning the normal gradients, as vapor transport largely occurs via diffusion, the normal growth rate R_n is proportional to the areal flux F_v to the surface

$$F_v = DN_{eq}\nabla\sigma \cdot \hat{n}, \tag{1}$$

where D is the vapor diffusion constant, $\hat{n}$ is the surface normal, and N_{eq} is the equilibrium vapor density at the local surface temperature. This means that a larger growth rate of a face implies a larger normal gradient, which should positively correlate to

15 a larger lateral surface gradient. Hence, taken together, the surface gradient in supersaturation that leads to hollowing, say on the basal face, will be weaker at low normal growth rates of the basal and weaker at high normal growth rates of the adjacent prism faces. That is, the growth on one face influences the lateral gradients on the other faces.
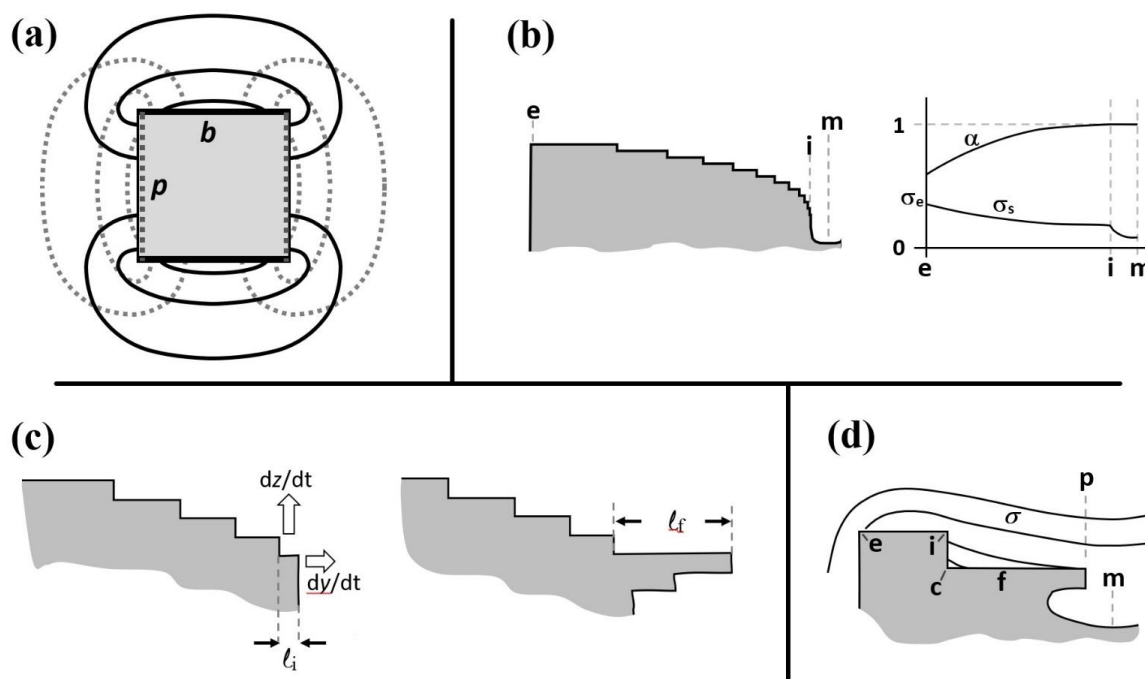
20 **Figure 13:** Processes involved in hollow close-off and terrace formation. (a) Basic patterns of vapor-density contours on a solid prism for growth only on the basal faces b in solid, dark curves, and for growth only on the prism p in dotted grey curves. The general case has a linear superposition. (b) Standard picture of hollow formation. Steps coming from edge at e become closer towards the inside edge i at right. Face middle is m. (Other half of face, as well as steps on side face, are not shown.) The plot on the right side shows the deposition-coefficient function α at top, with the trend in surface-supersaturation σ_s sketched below. (c)

Atmospheric
Chemistry
and Physics
Discussions

Close up of step-clumping region near inside edge **i** where the steps are separated by l_i. Protruding growth can occur towards the right (dy/dt), normal growth upward (dz/dt). Protrusion shown at right, last step length now l_f. (d) Supersaturation contours when a terrace **f** forms via lateral growth. Here, **c** is the inside corner, **p** is the protrusion.

5   The lateral surface gradient in supersaturation leads to hollowing via its effect on the surface steps (e.g., Frank, 1982; Nelson and Baker, 1996; Wood et al., 2001). Briefly, as sketched in (b), steps originate from the crystal edge **e** and flow towards the crystal center **m** on the right. The sketch on the right shows the trends of vapor supersaturation along the surface and deposition coefficient function α. Near the edge, the vapor supersaturation σ_e is relatively high and the steps are relatively far apart, but there is a relatively high fraction that desorb, which is described by its low deposition coefficient α_e. As the steps move toward

10   **m**, they slow down and become more densely packed, thus increasing the local deposition coefficient. At the edge **i** of the hollow, essentially all the incident molecules reach a step and the steps are clustered together to the point that they hardly move. A wall of steps builds up here, at the step-clumping region (SCR), forming the edge of the hollow. (Neshyba et al. (2016) proposed a more detailed model of step dynamics for ice, but it is not yet clear how a hollow would develop in that model.)

     However, after the hollow forms, the local supersaturations may change. This change could be due to either a change in

15   external conditions (e.g., temperature or supersaturation), a change in growth rate of a face due to a changing activity of the step source, or simply the increasing size of the crystal. For example, an increase in crystal size will generally decrease σ_e. Regardless of the cause, consider now the sketch in (c) in which a slight change in local conditions near the hollow edge **i** has occurred, causing a slight increase in the local step separation l. The normal growth rate dz/dt at **i** is the step height h divided by the step-passage time τ (time between successive passings of a step at **i**). The latter time is the step separation divided by the step speed

20   v_s. However, for a protrusion of thickness nh ($n \geq 1$) that starts into the hollow, the protruding growth rate $dy/dt = v_s/2n$, with the factor ½ due to the AST flux coming only from the top side. Comparing the two rates,

$$\frac{dy}{dt} = \frac{l}{2nh} \cdot \frac{dz}{dt}. \tag{2}$$

When the hollow first forms, l may be of order h. But with the increase in l, as sketched in (c), then dy/dt increases, further increasing l and thus further increasing dy/dt. Eventually dy/dt may greatly exceed dz/dt. Hence, in this very basic description,

25   some change in step spacing near the hollow may become unstable, leading to a protrusion that can continue to grow, eventually sealing-off the hollow into a center pocket. Initially, there will also be some direct vapor-flux to the side of the hollow at the lip, but this contribution to lateral growth would vanish due to shielding from the opposite side as the pocket closes off.

     This basic treatment neglects lateral supersaturation gradients and advancement of the crystal face. Briefly, these factors make sealing-off of a hollow less likely at higher growth rates because the initial protrusion will become left behind in a lower

30   supersaturation region as the rim grow higher. As the supersaturation drops, the protrusion grows slower, amplifying the effect. Also, as the protrusion grows inward, the supersaturation should decrease (except in the case mentioned next), thus hindering or possibly preventing the instability. Thus, the above suggests a hollow instability at low growth rates, but not at high rates.

     Concerning terracing, if the SCR develops nearer the rim and becomes elevated as in (d), the interior region **f** may flatten. This flattening would be aided by a reversed surface supersaturation gradient; that is, if the inside corner **c** in (d) becomes isolated in

35   an effective vapor shadow (height **i**–**c** exceeding the vapor mean-free path), then the steps in region **f** will speed up as they go towards the higher supersaturations near the center. This would produce an interior face that grows laterally, flattening region **f** into terrace features such as those in Figs. 11,12. (It may also drive protruding growth to make a center pocket as also shown in (d).)

     The growth of crystals with many terraces has been called skeletal or hopper growth, but the structure differs between that in

40   relatively squat hollows and that in narrow columns. Referring to Fig. 14, we call the former as terraced (a) and the latter as

banded (b). A sequence showing banding during growth at atmospheric pressure, −30 °C, and 8.8% supersaturation is in Gonda et al. (1985). Schnaiter et al. (2018) shows the banding in hollow bullet rosettes from clouds and Nakaya et al. (1958) shows numerous cases on hollow columns and sector-like forms. The bands are much denser in the latter forms. Indeed, terracing and banding are very common in natural snow and hoarfrost.
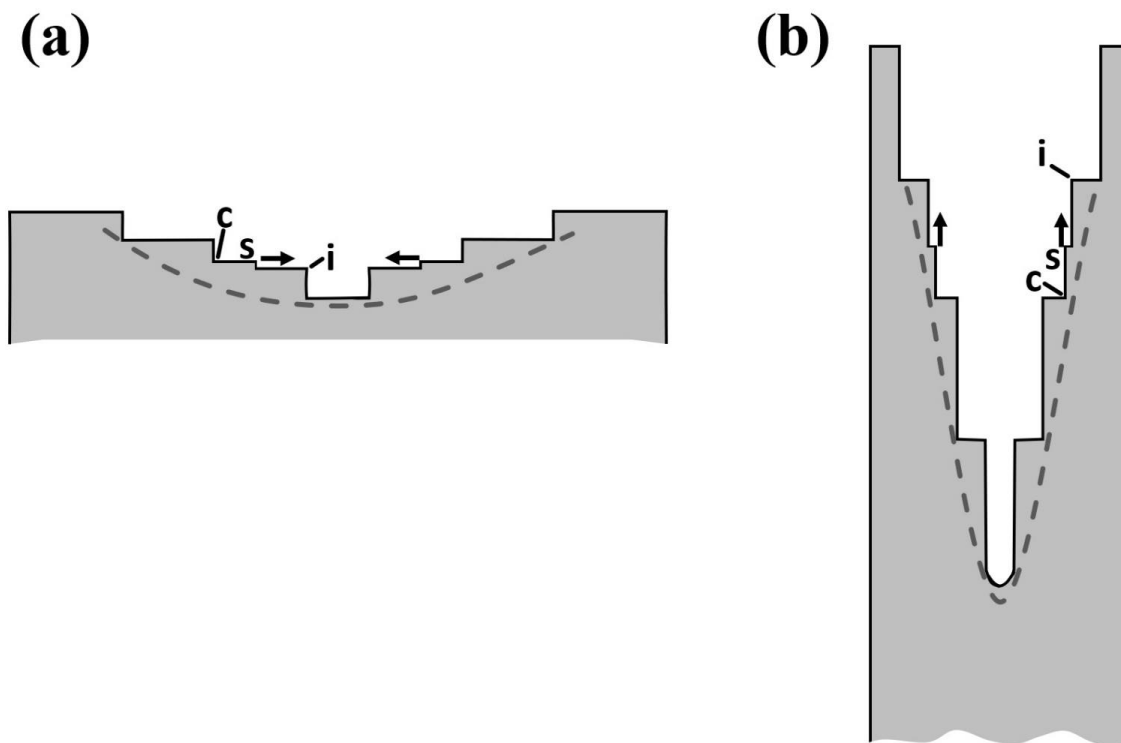
5

Figure 14: Terracing and banding in hollows. Sketches are cross-sections of top half of crystal, the dashed lines representing previous, smooth profiles. (a) A hollow on a squat crystal with terraces. On a sufficiently recessed terrace, the surface supersaturation increases towards the center from **c** to **i**, and thus step **s** speeds up as it traverses the face, flattening the terrace.
10 (b) A hollow on a long column or sheath. The large steps with inside corner such as **c** may produce the observed banding. A step **s** starting between **c** and edge **i** would speed up upon approaching **i**, flattening the band region.

Concerning the formation of a terraced hollow, initially, the inner surface may be smoothly curved, as shown in the dashed line in (a). Starting from such a smoothly curved surface, the closely spaced steps may clump into large step clumps as described
15 by Mason et al. (1963). In that process, once two steps become close enough to essentially lock together, they move more slowly, allowing steps further back to catch up. Mason et al. did not include supersaturation gradients, but such gradients may promote the clumping. In this way, a step-clump of two steps quickly becomes a clump of three, and the clumping continues. (Velikov et al. (1997) describes a more complex interaction for step-bunching.) Once a sufficiently tall clump forms, any step **s** between an inside corner **c** and an edge **i** would speed up as it approached **c**, flattening the terrace as described above.

20 The banding in a narrow column in (b) similarly starts with a smooth curve, and may form a macrostep by the same step-clumping process. But in this case, a step **s** flows from the center out towards the higher supersaturations at the rim. Thus, a step clump at **i** does not need to be high before the flattening effect becomes large because in this case the step is speeding up due to

the higher supersaturation even without an edge at **i**. As with the terracing case, as **i** grows, it sticks out into regions of higher supersaturation, meaning that the next step may travel even faster. Thus, a later step overcomes a previous step, quickly building up a larger macrostep, which would appear as a band in the hollow. New bands would form via the same process as the crystal grows, leading to a series of nearly equally spaced bands.

5   This treatment suggests that step sources and dynamics, protrusive growth, the moving interface, and the shape of the supersaturation contours all likely influence hollow structure, leading to their highly variable behavior even under constant growth conditions. A similar process of banding may also apply to the 'cross-rib' features (Nelson, 2005) on the backsides of branches on broad-branch and sector-plate crystals. The suggested mechanism in that study was instead changes in temperature or supersaturation around a crystal. These changes would cause the width of the branch to vary, and the same process may also
10 produce some terracing and banding in hollows by temporarily changing the rim width **e–i** in Fig. 13d. That is, more than one mechanism may alter the hollow structure.

3.11 Cause of pocket-size variability

Consider the variability of the hollow sizes and shapes under low normal growth rates (e.g., on different faces of the crystals in Figs. 11 and 12). Such variability is uncommon at high growth rates, so we outline here a few factors that may play larger roles
15 at the low growth rates at low supersaturations. One factor is the greater variability in the normal growth rates. In contrast to high-supersaturation growth, the step-sources at low supersaturations are thought to be crystal defects such as dislocation outcrops and stacking faults. The dislocation activities will in general be different on different faces of the same crystal, and between different crystals, and also may change during growth. But other factors may lead to greater variability at low supersaturation. For example, the greater relative role of lateral growth processes at low normal growth rates leads to the
20 phenomena described in the previous section; that is, the interplay between the surface influence and the bulk vapor-diffusion influence may allow more complex nonlinear feedbacks on growth, leading to a greater chance of unstable behavior. This variability may be increased by the variation in dislocation activity, which would have a larger influence at low supersaturation because the surface has a larger direct influence on growth rates under these conditions. Finally, after a given duration, the smaller crystal sizes at low growth rates mean that variability in the initial droxtal size and properties would have a relatively
25 larger influence on the crystal form.

In contrast to the other low-supersaturation crystals shown here, the six planar pockets in Fig. 3 are remarkably similar. The reason for the pocket symmetry is likely due partly to the equal normal-growth rates of all six prism faces. This symmetry in the growth rate must arise from having the same step source on all faces. Given that the crystal has an apparent stacking fault or stacking-disordered region that intersects all prism faces, the obvious step-promoting defect would be the fault. Fault-generating
30 steps had been proposed by Ming et al. (1988) via a mechanism in which the fault yields a lower barrier to layer nucleation. Thus, we suggest that the six pockets open-up at the same time because the step-generation mechanism is the same stacking-fault mechanism on all six faces, producing the same normal growth rates on all faces. (That the fault could both be a source of growth and a location of hollowing is harder to explain, but possible given that the steps would start from the prism–prism edge, not the hollow location.) Concerning the hollow closing-off to form pockets, two factors occur during growth that will likely
35 change the step-separation near the pocket, thus determining whether they close-off. One, the edge supersaturation decreases due to the larger crystal areas, and two, the relative position of the pocket-opening changes on the prism face due to one basal face growing faster than the other (i.e., the side-view in Fig. 3d shows greater advance of the right basal face than the left). As both of these factors will be equal for all six prism faces, the closing-off should occur at the same time, leading to the identical nature of

the six pockets. Finally, note that the groove region, which is sublimation-rounded like the edges, did not produce a pocket during re-growth like the corners. The reason for this may be the much smaller radius of curvature in the former case.

3.12 Two-level planar formation on droxtals, the droxtal center

Protruding growth occurs on some frozen cloud droplets, or droxtal, causing them to directly sprout thin basal planes, leading to
5 the two-level tabular crystal also known as crystal types P2-P4 (hereafter, we refer to the crystal-type classification in Kikuchi et al. 2013), that retain the boundaries of the original droxtal in the center. Takahashi and Mori (2006) show several cases of such sprouting. Their process of formation has already been described by Yamashita (2014) as a case of protruding growth, but we include it here due to its close relation to other phenomena we describe. See Fig. 15 for several examples of the two-level protrusions on large droxtals as well as single protrusions on rime droxtals.
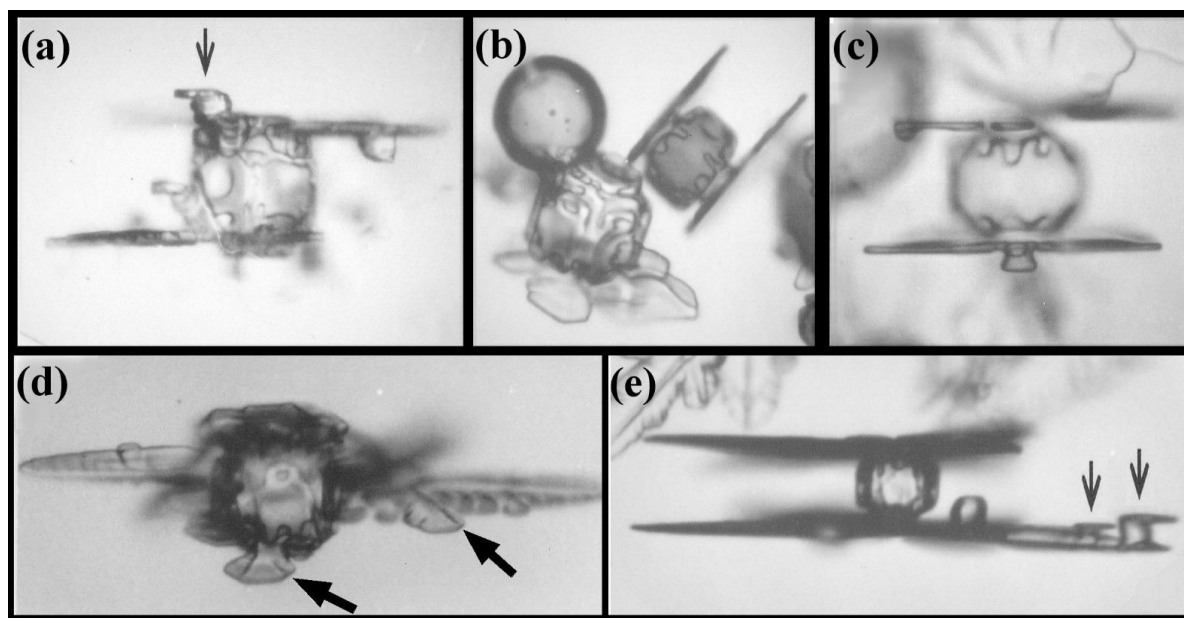
10

Figure 15: Protruding growth on large droxtals (~40–70 μm) to form the two-level structure. Black arrows in (a) and (e) show protruding growth on smaller rime droxtals. Black arrows in (d) shows complex structure of branch and sidebranch backside. (From the cloud chamber.)

15

The sprouting transition, shown in Fig. 16, can occur in the tabular-growth regime (within a few degrees of −15 °C), where, soon after freezing, the surface supersaturation quickly drops to a value that greatly suppresses layer nucleation on the basal faces (Nelson and Knight, 1998). Thus, after the basal facets form on the top and bottom of the droxtal (a–b), they mainly grow laterally. (Some prism facets also should form, but are not important here.) The growth continues as protruding growth in (c), as
20 was the case for corner pockets. But, unlike the corner-pocket case, protruding growth does not occur on the prism faces (or, at least is much slower), and thus the basal protrusions extend out from the boundaries of the initial droxtal, creating two levels. Sketch (d) shows one level grows more than the other, which is due to asymmetry in the vapor-diffusion field around the falling crystal (Fukuta and Takahashi, 1999). As shown in Fig. 15a, and found much earlier by Nakaya (1954), branches can also occur on both levels.
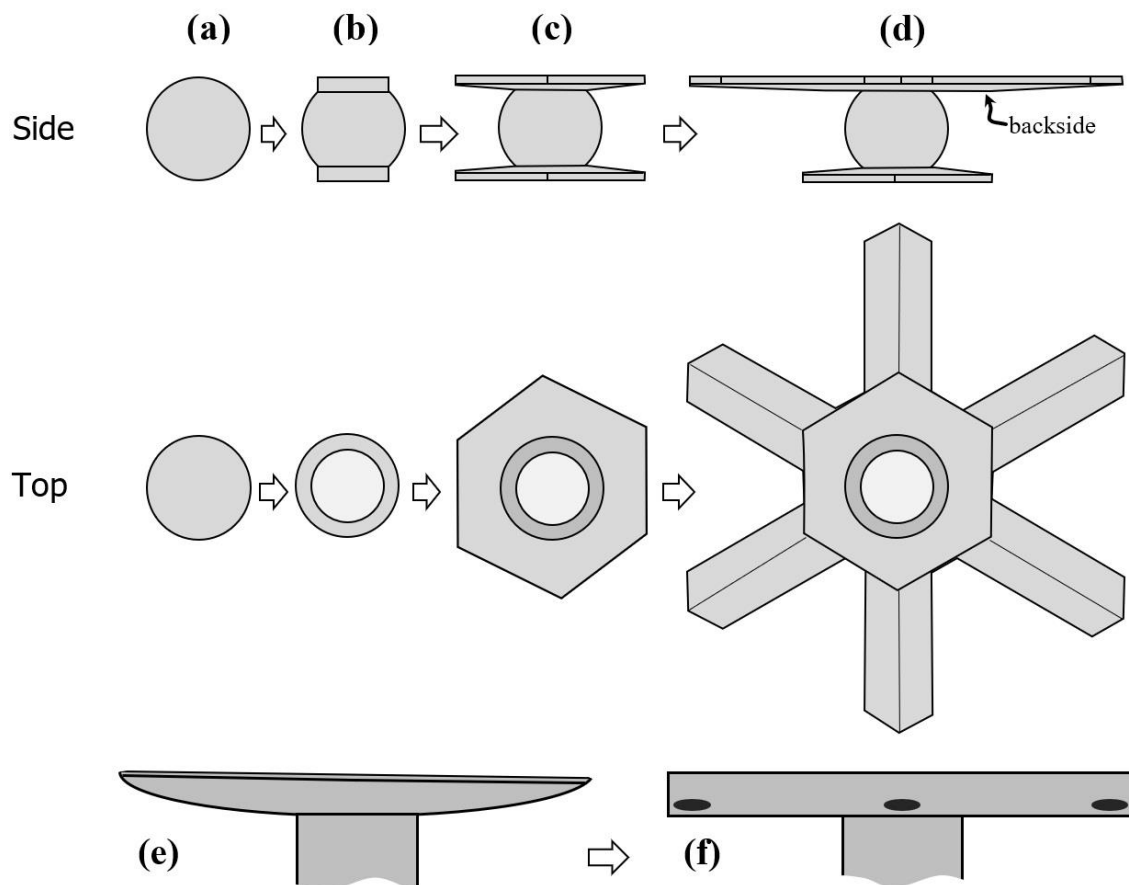
25

Figure 16: Lateral and protruding growth on a droplet or column under constant or varying conditions. (a)–(d) follow the description first given by Yamashita (2014). Here, the growth on a frozen droplet leads to protruding growth and a two-level snow-crystal. Compare side image in (d) to images in Fig. 15, the top image to the snow-crystal shown in Fig. 7c. (e) Cap on one end of frozen droplet or column, showing rounded backside. (f) Same cap after a decrease in growth rate, allowing corner pockets to form. Details of the process between (e) and (f) are not shown, but would be the same as that shown in Fig. 8 except that only one side of the crystal is rounded. This latter process may explain the observed line of pockets on the crystal in Fig. 7c.

Such abrupt sprouting can explain the small center circle observed in some branched snow crystals (e.g., Fig. 7c). Not all branched, two-level crystals show such a "droxtal center"; such cases likely arise instead via the process first described in Frank (1982) (later modified in Nelson (2005) to fit observations of Yamashita (1979)). Bentley (1924) wrote that "at least half" of the 4200 crystals he had photographed in 40 years had such a center circle, and argued that it was the frozen droplet (droxtal) upon which the crystal formed. What factors may cause the droxtal sprouting in some cases but not others? Yamashita (2014) observed sprouting on larger-than-average droxtals. Large initial droxtals may favor sprouting because their larger areas would depress the surface vapor density more than that of a much smaller droxtal, essentially shutting off the normal growth on the basal face. This effect of size may also lead to a greater vapor-density gradient where the protrusion starts, particularly at higher ambient supersaturations that would tend to produce higher σ_e at the face edge. In addition, the AST flux should be higher when the basal face has larger x_s values. Mason et al. (1963) found x_s to peak in −9 to −15 °C, a temperature near which such two-level

Atmospheric
Chemistry
and Physics
Discussions

Open Access

crystals sprout. In the recent vertical wind-tunnel experiments of Takahashi (2014), nearly all the images of planar snow crystals clearly show the center droxtal as described here. In those experiments, the crystal nucleated and grew in a droplet cloud of various liquid-water contents. The mean droplet diameter (before freezing) was 8 μm, but inspection of the images indicates that the droxtals that sprouted the two-level crystals had a slightly larger diameter (~9–13 μm). Thus, both relatively high initial

5   supersaturations and relatively large droxtals may favor two-level initiation via protrusive growth.

3.13 Corner pockets on rounded tabular backsides

The snow-crystal image in Fig. 7c appears to show corner pockets on both levels of a two-level crystal. In addition, the smaller inset shows a sequence of small circles along the centerline of a branch, a pattern reproduced on the other branches as well, ruling out the possibility that these are rime. Similar series of circles appear in crystals #11, 12, and 22 in Bentley (1924). In

10 most cases, the circles appear before the crystal branches sprout. These circles may be corner pockets by the following mechanism. During growth, the backside of the plates and branches of two-level crystals show rounded features even without sublimation (c.f., Fig. 15d, Shimada and Ohtake, 2016). Instead, a short slowdown in growth may allow lateral and protruding growth from the rounded region via steps similar to those shown in Fig. 8b–e, but on one side only. Also, the protruding growth from the side is more difficult to picture due to the positioning on a ridge. Nevertheless, the basic process may be like that

15 sketched in Fig. 16e–f. If correct, the existence of each pocket marks the time when growth temporarily slowed down.

3.14 Capped columns, multiple-capped columns, and florid crystals

Capped columns (CP1a, CP1b) form when a crystal grown at near water saturation in a column regime quickly moves into a region of temperature in a tabular regime. The form is similar to the droxtals with two levels, as in Fig. 15, but with a column between the two basal extensions (e.g., a simple plate or dendritic plate.) One model of their formation involves an extreme form

20 of hollowing in which the step-clumping region (SCR) forms near the step origin at the corners (Nelson, 2001). However, that model cannot readily explain the capped columns with central thin basal extensions, also known as multiple-capped column (type CP1c). Instead, the similarity to the two-level case in Fig. 16 suggests an AST contribution to cap formation. If so, what is the source of the originating basal plane on the interior of the column for the CP1c case?

The basal protrusions on rime in Fig. 15a,e (narrow arrows) suggest one possible source of an interior basal extension. As

25 sketched in Fig. 17a (top), a rime droxtal could develop a basal face aligned along that of the column (assuming the droplet freezes with the same orientation). The face would grow laterally and then protrude via AST as shown in (b). Once the basal extension starts, it can grow both outward and around much of the column. If the two end caps have a head-start on growth, the rime droxtal nearest the center, being further from the competing vapor sinks, would have a greater vapor flux and thus be more likely to grow out into a larger basal extension. (Otherwise, two basal extensions may form relatively close together, competing

30 for vapor until one grows significantly larger, stunting the other.) The image labeled CP1c in Fig. 1 of Kikuchi et al. (2013) shows other rime droplets along the column, suggesting this mechanism. Without the rime, it may be unlikely that a high density of new layers could nucleate in the middle of the column, produce an SCR, and sprout a new plate. Moreover, most cases of CP1c have central basal extensions that are not in the exact center, thus suggesting a random element such as riming.
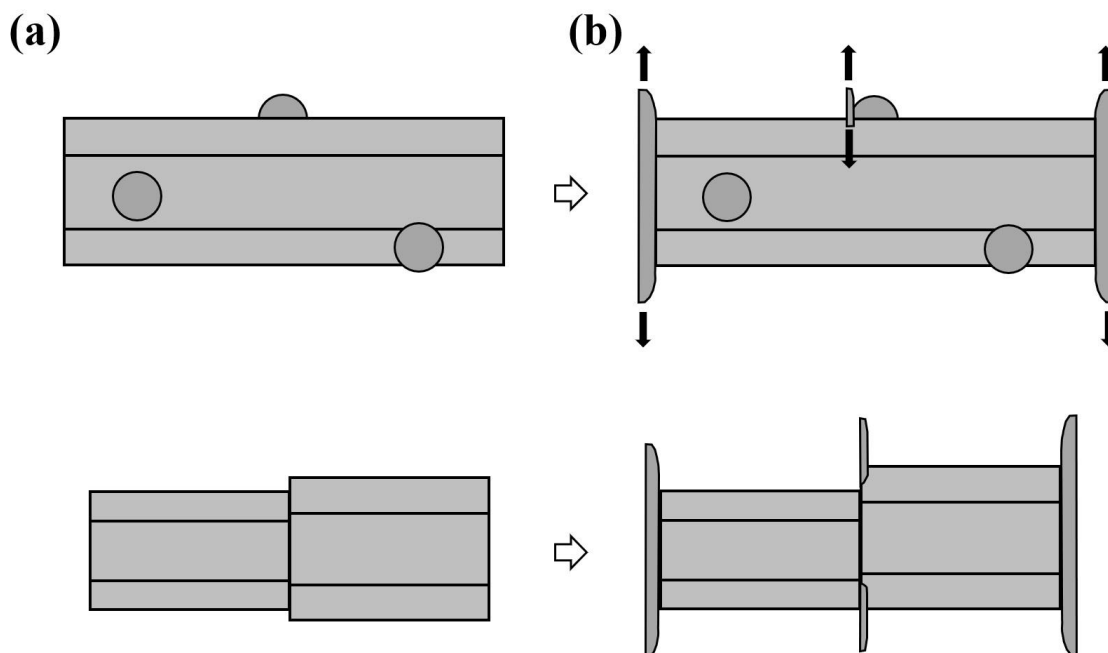
Atmospheric
Chemistry
and Physics
Discussions

(a)   **(b)**

Figure 17: Protruding growth leading to multiple capped-column crystals. (a) A columnar crystal either with rime droplets (top) or some sort of break feature (bottom). (b) Moving into a tabular-growth temperature leads to protruding tabular growth. Black arrows in rime case show that the protruding growth extends outwards in all directions within the plane.

5

In addition, the examples of CP1c in Magono and Lee (1966), plate 16, show examples in which the columns differ on either side of the center basal extension and do not show evidence of rime. In these cases, the column likely already had an interior basal plane upon which to sprout the extension before the conditions changed to a tabular regime (e.g., Fig. 17, bottom). Although we know neither how common such crystals are nor how the interior planes arise, but we know they do occur as the

10   crystal in Fig. 9 demonstrates. Such an interior basal plane could also arise from a small bundle-type column such as a bundle of needles (C1b) or bundle of sheaths (C2b), which are discussed in §3.19. Other cases include a column with a small double-twin (e.g., Kobayashi et al. 1976, section 4.10), crystals such as those in Fig. 12 (possibly twins), columns with prism hollows, or a column that underwent previous transitions in the tabular regime.

Similar to the capped columns, the protruding growth process may also influence the initiation of tabular extensions on 'florid'

15   crystals (Bacon et al., 2003). The base crystals (before sprouting) are squatter than the columns for the capped columns, and sometimes polycrystalline. See type P8b 'complex multiple plates' (Kikuchi et al. 2013). Also similar to the capped columns are the bullets with plates (CP2c), which probably form by the same processes.

3.15 AST contribution to normal growth rates of thin plates, dendrites, needles, and sheaths

To estimate the contribution of the AST flux to lateral-type growth, consider a simple treatment based on the BCF (Burton et al.,

20   1951) model of crystal surfaces. Assume here that the region over the face edge (i.e., the lateral-growth front) is rough, and thus this region can be treated as BCF do for a step edge, that is, as having an equilibrium concentration of mobile surface molecules.

Atmospheric
Chemistry
and Physics
Discussions

Assume further that, as suggested by step-motion experiments (Hallett, 1961), molecular migration over the edge encounters no barrier. In this case, straightforward use of BCF gives a flux of molecules f_L (per edge length) that equals

$$f_L = x_s \frac{v}{4} N_{eq} \sigma_e , \qquad (3)$$

where x_s is the surface migration distance, v is the mean molecular speed in the vapor, N_{eq} is the equilibrium vapor density, and

5   σ_e is the vapor supersaturation near the edge. This result suggests that we can view the adjoining face region within x_s of the edge as a collection region of molecules impinging from the vapor. Assuming that this face edge has n adjacent facets from which to draw the flux, and the edge has thickness t over which the AST flux is distributed, the effective flux (per area) F_{AST} is

$$F_{AST} = n \frac{x_s}{t} \frac{v}{4} N_{eq} \sigma_e , \qquad (4)$$

an amount we compare to the direct vapor flux F_v (e.g., Nelson and Baker, 1996),

10    $$F_V = \frac{v}{4} N_{eq} \sigma_e . \qquad (5)$$

where the deposition coefficient is assumed to be unity (effectively rough surface), consistent with the assumption of a step edge in the derivation of Eq. (3). Thus, as a crude estimate, the ratio of AST flux to standard vapor flux is just $n \cdot x_s / t$, with $n = 1$ or 2 depending on whether the thin edge is bound by one facet, as in a dendrite branch, or two facets, as in a thin disc. In general, n can vary between 1 and 2 when two faces meet on one edge, such as the two prism faces along the edge of a sheath, and may

15   exceed 2 in the case of a thin whisker. In the next two subsections, it will be convenient to view the total flux as equivalent to having an effective supersaturation of $\sigma_{eff} \equiv \sigma_e \cdot (1 + n \cdot x_s / t)$.

Concerning x_s / t, early estimates of x_s from step-motion experiments on the basal face gave a range of values, depending on temperature, of about 1–6 μm (Mason et al., 1963; Kobayashi, 1967). A more recent measurement gives a value of about 5–10 μm at −8.6 °C (Arakawa et al., 2014). For the thickness t, a recent study shows that the tip region of a dendritic snow crystal has

20   a tapered tip (Shimada and Ohtake, 2016; 2018). The measurement does not give a precise value of t exactly at the edge, but an average value within ~10 μm of the edge gives about 0.3 μm. Thus, the estimates of x_s / t here suggest that the AST flux could be up to ~3–60x the direct vapor flux in certain cases. The resulting increase in growth rate from this flux would be less than this factor due to the vapor-diffusion process. Also, the analysis in Appendix B suggests that a partial barrier to migration over the edge may exist, and the resulting reflection of some admolecules at the edge would reduce this AST flux. Nevertheless, such a

25   flux could significantly increase the rate of growth (maximum dimension) of thin planar growth forms such as the dendrite (P3b) and fern (P3c) crystals, as well as sheath (C2) and needle (C1) forms.

3.16 Rounding of plates and tips of fast-growth forms

Fast-growing crystals have leading growth fronts that can appear rounded, and some thin tabular crystals can be disc-shaped or scalloped. For example, the sheath extensions in Fig. 18 include some with tips that appear rounded and some that appear flat-

30   faced. Similarly, Knight (2012) observed sheath-needles with rounded tips. Sei et al. (2000) shows rounded sheath-needles sprouting from prism corners that later flatten upon becoming larger. An increase in supersaturation would then cause smaller, round tips to sprout on the larger, flat tips. Round tips also seem to appear on the faster-growing dendrites near −15.0 °C (P3b,c). Gonda and Nakahara (1996) even found such rounding on dendritic crystals grown with their basal face against glass. (However, for the fast-growing dendrite cases, the small scale of the tips makes it hard to discern small facets with limited image resolution,

35   and a slight amount of rounding may quickly occur in brief undersaturated conditions, so the phenomenon is not well-established yet.) Away from the tip, rounding of the side vertices has been attributed to SCR forming due to decaying gradient in surface supersaturation (Nelson, 2001; Frank, 1974). In slower-growing tabular crystals, Keller et al. (1980) observed disc crystals faceting as they became larger and thicker, as did Knight (2012). In our previous experiments (Nelson and Knight, 1996), we

Atmospheric
Chemistry
and Physics
Discussions

also saw small disc crystals develop facets as they grew (Nelson, 2014). Also, Yamashita and Asano (1984) grew rounded tips of "serrated" dendrites at about −2.0 °C, and noted that they were thinner and grew faster than the thicker, facetted tips around −3.0 °C. Thus, rounding can occur in several situations. But, as argued in Nelson (2001), the supersaturations are too low for the phenomenon to arise from kinetic roughening, so we ask if AST may drive such rounding.
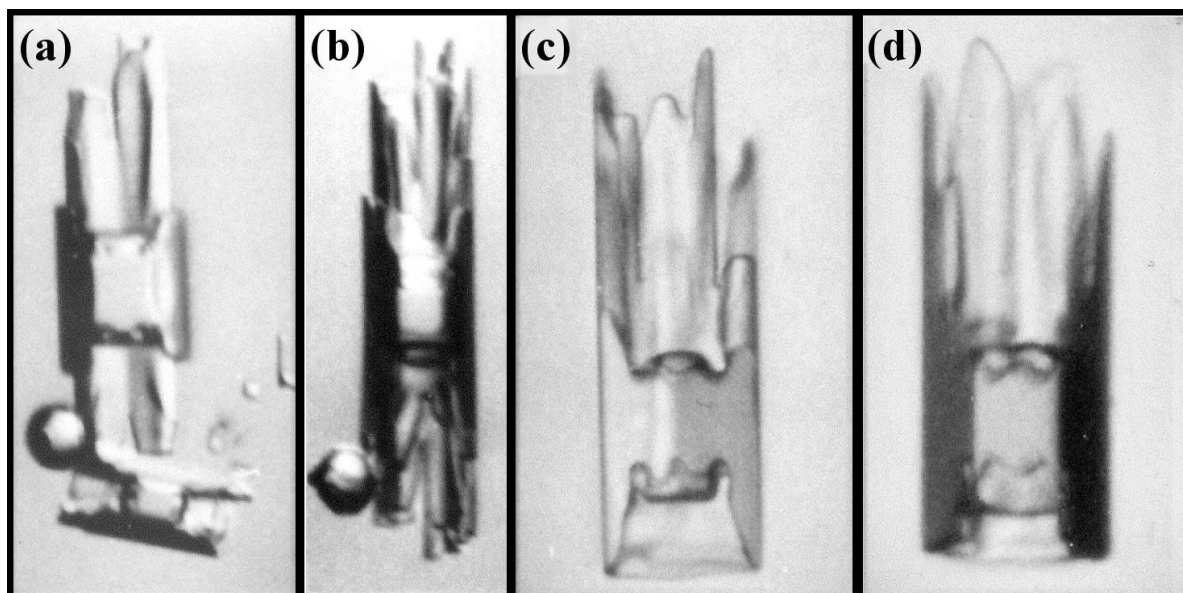
5

Figure 18: Initial sheath protrusions sprouted from droxtals of ~40–70 μm diameters at −4.8 °C (a,b) and −5.9 °C (c,d). (From the cloud chamber.)

10   Consider first a thin tabular crystal with two basal faces, focusing on the region near a prism–prism edge as sketched in Fig. 19a. As shown in the top sketch, the collection area for AST flux at the tip **c** has an angle of just 120° compared to the 180° further down (at least a distance of ~x_s) at **e**, making the AST flux ~2/3rds the value at the tip. If the total molecular flux is dominated by the AST flux, then this effect would move the point of highest total flux away from the tip. Equivalently, we can view position **e** as having higher effective supersaturation than **c**. Thus, as shown in the bottom sketch, the point **e** of new-layer

15   nucleation has moved down from the tip. Moreover, if the edge region is effectively rough, then the regions of higher effective supersaturation will advance faster than regions with lower values, changing the vertex or tip shape until a steady-state shape emerges. Such a shape would be rounded, as shown in the sketch. Thus, if the crystal edge is nearly rough, then AST flux can cause the corner or tip to round as steps travelling from their source at **e** to further down the tip toward **c** can readily clump. In this case, $n = 2$ due to AST flux from the top and bottom basal faces. Thus, the edge plan view may be similar to that shown at
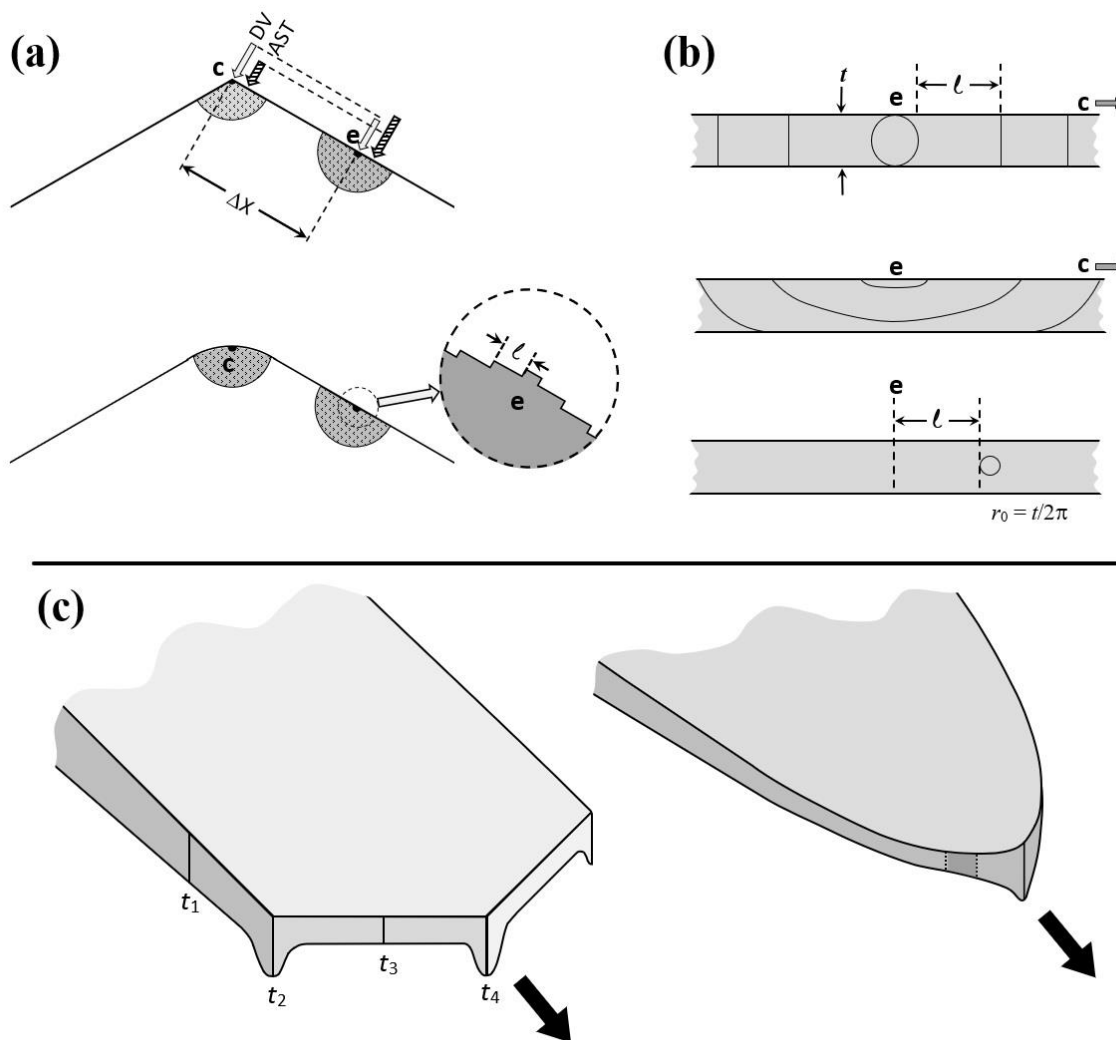
20   the top in Fig. 19b.

Figure 19: AST-induced rounding. (a) Direct vapor flux DV and AST at the corner **c** and edge **e** of a thin tabular crystal. Shaded regions are effective collection regions for AST flux, arrows show relative magnitudes. Inset at bottom is shown in top case of (b). (b) Nucleation and step flow on edge region of thin crystal in (a), plan view of edge. Top sketch is symmetric case. Layer-nucleation point **e** of (a), has steps moving away with initial separation l. Middle sketch shows asymmetric case leading to step separation $l \sim t$. Bottom sketch is step configuration used in calculation in Appendix B. The small circle is a closed step loop, used to approximate collection by a straight step of length t, the crystal thickness. (c) Thin-branch case with non-crystallographic backside. Thickness t is greater at the vertices t_2 and t_4 and thus has less growth from AST flux. Rounded case at right with small prism face bound by dotted lines.

A dendrite branch has a different tip shape, with the edge prism faces bound by just one basal face, the other being non-crystallographic. Thus, the edge plan view may be more like that in the middle of Fig. 19b. In this case, a second factor may cause the vertices to round. As sketched in (c), the leading prism faces are expected to be thicker at the vertices, that is, $t_2 > t_{1,3}$ and $t_4 > t_3$. (Although the thickness variation right at the perimeter was not detected by recent interferometry studies (Shimada and Ohtake, 2016; 2018), the formation of a main ridge and side ridge, which are clearly visible in nearly all tips, appear to

require such an increase in thickness.) Their formation mechanism, as described in Nelson (2005), relies upon the influence of the direct vapor flux. But if their growth is also significantly influenced by AST flux, and they are thicker at the vertices, then Eq. 4 shows that their growth rates will be slower. In this case, they may advance more slowly at the vertices, leading to the rounding shown in (c).

5   These rounding mechanisms depend upon the prism faces being nearly rough. Section 3.22 discusses various mechanisms for such roughening, but one possible factor is illustrated by the middle sketch in Fig. 19b. Here, layers nucleate at one basal–prism edge and can reorient parallel to the edge with a separation l of roughly the crystal thickness t, which may make the edge effectively rough. For a face to essentially collect all surface ad-molecules, the step spacing l need only be smaller than x_s. But if the spacing becomes significantly smaller than x_s, the normal growth rate becomes proportional to the local effective
10   supersaturation (as all the flux is incorporated into the crystal), meaning that a decrease in this supersaturation would cause the surface to respond, producing rounding. Such a case is akin to the kinetic roughening that is driven by high supersaturations (Elwenspoek and van der Eerden, 1987), but in this case the supersaturations are too low.

Although AST is a likely factor in some of these cases of crystal rounding, rounding in general on vapor-grown ice is more complex than the simple arguments above. Crystal rounding on vapor-grown ice may involve a combination of AST,
15   supersaturation gradients, defects, and perhaps yet undiscovered factors.

3.17 Tip shapes of sheath and sharp needles

Other aspects of tip shape may also influence the normal growth rates of needle crystals. Needle crystals (C1a) are long, thin, columnar crystals with "tops shaped like a knife edge" (Kikuchi et al., 2013) that form near −5 °C. In their initial growth, they appear as narrow prism planes that sprout from the edges of the basal plane, similar to the sprouting of basal planes during the
20   formation of two-level crystals (§3.12). Examples shown in Fig. 18, as well as in Sei et al. (2000), suggest that they initiate via protrusive growth. Knight (2012) observed both sheath-needles and, less often, a newly reported type he called sharp needles. The sheath needles would grow at a rate of about 0.3–1.0 μm/s, whereas the sharp needles grew about twice as fast, about 1.5–2.5 μm/s. The sharp needles also had a smaller diameter and appeared more nearly round in cross-section. Why did they have different tips and why the distinct growth rates?

25   The different tip shapes may be the reason for the bimodal growth rate. Given that both needle tips are likely to be of order 10 μm or less, the AST flux is likely to be significant, perhaps even dominant. The net effect of this flux should depend on the ratio of the collection area (on the adjoining prism faces) to the growth-front area. Consider the two tip shapes at the bottom of Fig. 20. The left appears to be the same as the sheaths in Fig. 18, whereas the right has the angle like that of "iii" in the right scroll of Fig. 21b in which one prism face is missing. If the arrows represent the AST flux, then the right case of Fig. 20 has almost twice
30   the AST flux to the growth-front area (dashed circle) than the left case; that is, n is near 1 on the left, but almost 2 on the right. Thus, this shape may lead to nearly twice the growth rate as the other. Another factor is the influence of the backside of the tip on the surrounding vapor density. The backside, being non-crystallographic, is effectively rough and thus efficiently draws in vapor. Neither the front-side prism faces ($p_1 p_2$ or $p_1 p_5$) nor the tip are collecting much mass from the vapor. But for a given length of needle, the open sheath on the left has a greater backside area than the proposed sharp needle on the right. This
35   backside may dominate the mass-uptake, just as it appears to do on dendritic crystals (Nelson, 2005). With the smaller area for the sharp-needle case comes a smaller mass uptake, and with a smaller mass uptake, a higher surface supersaturation and higher normal growth rate. In this way, the sharp needle may grow nearly twice as fast as the sheath needle, as was observed. Consistent with this argument, when the temperature of the sharp needle was raised to slow down growth, it thickened enough to discern

Atmospheric
Chemistry
and Physics
Discussions

that it had a triangular shape (Fig. 4 of Knight, 2012). This 60° interior angle of the proposed sharp needle is a feature of trigonal crystals. In §3.21, we argue that this angle is stable in the columnar regime, which includes the needle case.
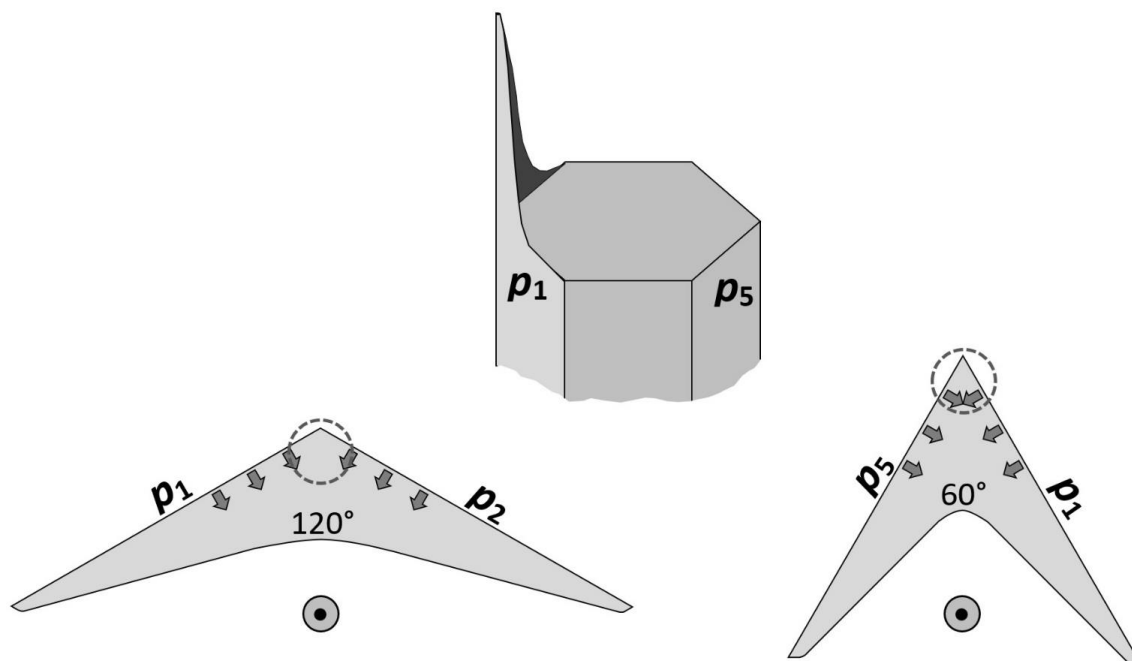

5   **Figure 20:** Needle-tip cross-sections. Prism face p_1 through p_6 run clockwise around crystal sketch in middle-top. Bottom shows views looking straight down. Left: case from sheath with prisms p_1 and p_2. Right: case from sheath initially with prisms p_1, p_6, and p_5, but middle prism p_6 vanished. Arrows show AST flux from adjoining prism faces.

3.18 Influence of AST on scroll crystal features

10   A perplexing growth feature is the scroll (C3c). With a scroll feature, thin prism-face "sheets" or side-planes tend to curl inward while maintaining a prism orientation, somewhat resembling a paper scroll as shown in Fig. 21. (For formation sequences, see Figs. 3 and 5 in Sei et al., 2000.) In the atmosphere, the original Nakaya diagram (e.g., Nakaya et al. 1958) shows scrolls forming at and above water saturation near −7 °C, which is consistent with later diagrams by other authors. Later, Nakata et al. (1992) found scrolls to be very common features of certain polycrystals (Gohei twins, CP7a). But perhaps one of the earliest
15   descriptions of a scroll is in Seligman (1936), where he finds large examples in crevasse hoar. However, with the aid of a standard macro lens on a common digital camera, one can observe them frequently in hoar frost. A description of their formation is briefly mentioned in Higuchi et al. (2011), but their proposed mechanism differs from that presented next.
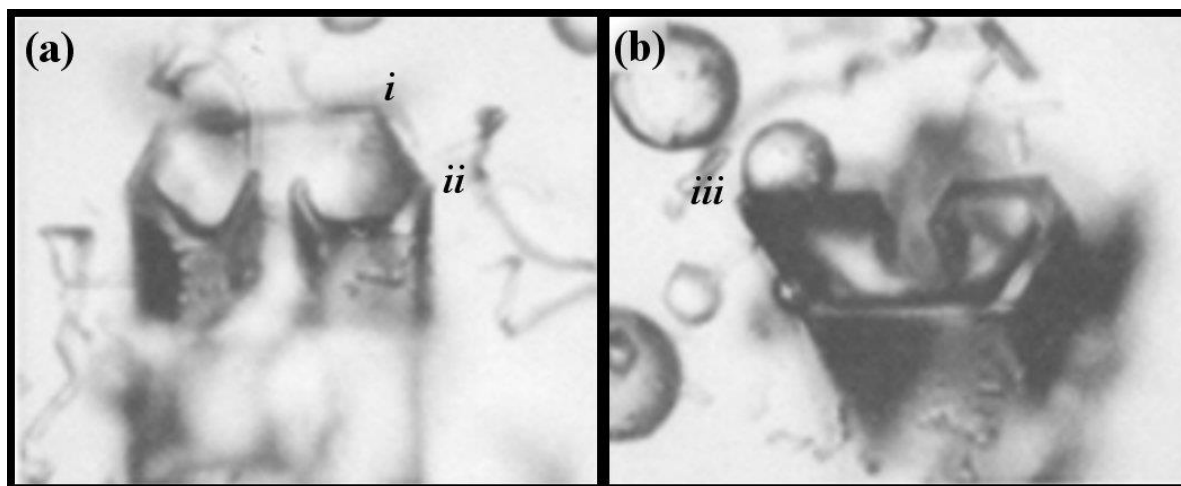
Figure 21: Scrolls formed on crystals of approximate diameter of 60 μm. (From the cloud chamber.)

The scroll may start as a protrusion, like a sheath, except on a larger-area basal face as shown in Fig. 22a. When this protrusion
5   is thin, it can grow rapidly because the AST flux is depositing onto a small-area region at the growth front. (Growth may be more
rapid normal to the page, but we focus on the side growth.) This rate is marked by the large arrow pointing across prism p_2 in (a).
But normal growth is also occurring on the backside (or inside), causing it to gradually thicken. (In this description, we assume
that the backside, or inside, of the scroll is mostly non-crystallographic.) This normal growth rate is marked by the smaller arrow
pointing down, towards the basal interior. On the leading front of the protrusion, direct vapor flux is also contributing to growth,
10   but when the feature is thin, this flux is overcome by the larger AST flux from prism p_2 (Eq. 4). Eventually though, this
protrusion thickens enough to reduce the protruding growth rate, at which point lateral growth on the front can form prism facet
p_3 there, essentially ceasing the lateral growth of p_2 as shown in the sketch. Now the process starts on the edge of these new
prism faces, causing new protruding growth at 60° to the old protrusive growth as shown at right, and the process repeats, later
curling around another 60° into a scroll-like shape. Each new "wing" of the scroll may have a smaller area due to it moving
15   interior of the structure where the vapor density is less, and thus the protruding growth rate is less. This process would lead to the
observed curling feature of scrolls. Compare vertices *i* and *ii* in Fig. 21a and Fig 22a.
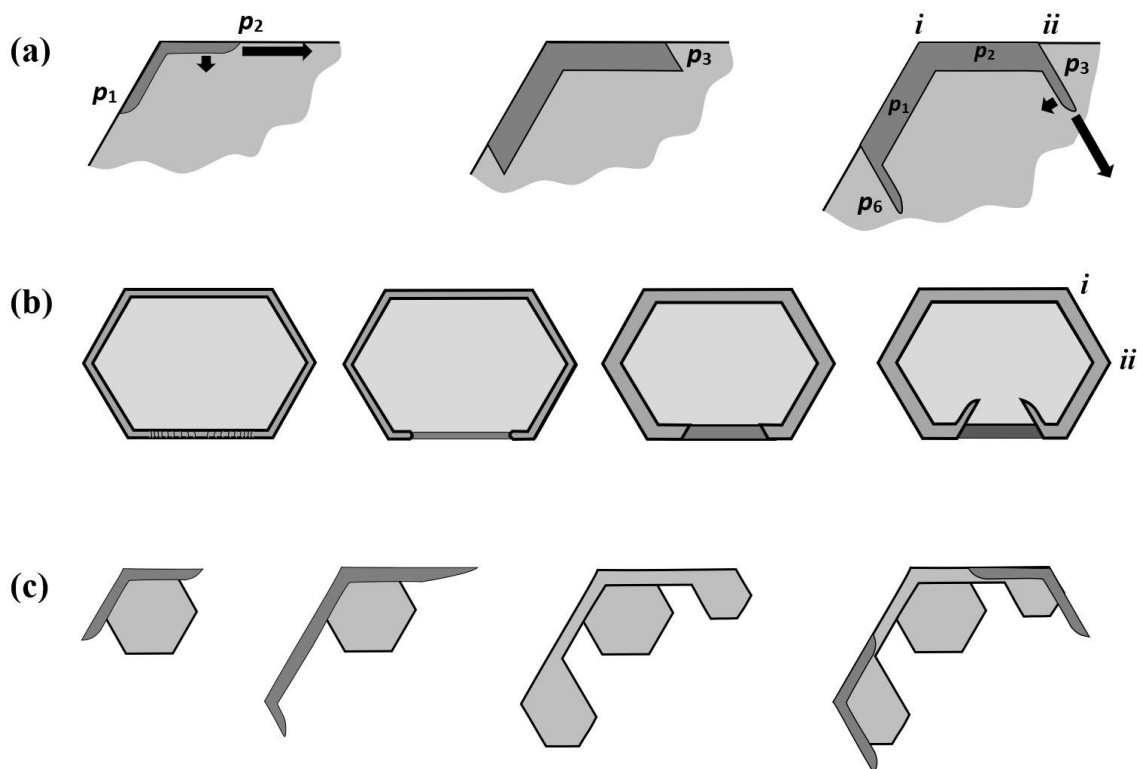
Atmospheric
Chemistry
and Physics
Discussions

Figure 22: Scroll and sheath bundles via protruding and normal growth. (a) The basic process, viewed along c-axis (normal to basal). The darker region is a sheath protrusion from prisms p_1 and p_2 going up out of the page. Arrows indicate relative rates of growth in width (via AST) and thickness (via normal growth). In middle sketch, protruding region has thickened, slowing the rate of protruding growth, allowing significant lateral growth on the ends that leads to new prism facets p_3 and p_6. In the right sketch, protrusion growth occurs on these new prism faces. The process can continue (not shown), generating facets p_4 and p_5. Compare *i* and *ii* vertices to ones in Fig. 21. (b) A complete sheath has its rim broken at the bottom (left), due to a vapor-density gradient or asymmetry. The process in the next three sketches follows the same process as explained in (a). Vertices *i* and *ii* correspond to those in Fig. 21. (c) Possible source of sheath and needle bundles from protruding-growth overshoot. Leftmost sketch follows from start of case (a) except protruding growth overshoots the base. (Overshooting is exaggerated to clarify the concept.) In middle sketches, the edge of the protrusion thickens and facets as in case (a). Far right, process repeats.

A scroll may also initiate from a cup-type crystal form or sheath (C2a) after part of its rim forms a break, which may in turn be due to an axial asymmetry in the nearby vapor-density field. As sketched in Fig. 22b, the sides of the break (at bottom) could then curl around via the same process as that sketched for (a). Supersaturations high enough to produce cup crystals are rare in the atmosphere, but are very common near hoar frost. As hoar cup crystals tend to be closely clustered, and thus having large local variations in vapor density, this initiation process may be likely for hoar scrolls. Large examples of this type are in Knight and Devries (1985). This case also more closely resembles that in Fig. 21a.

3.19 Bundles of sheaths and needles

Another perplexing growth form is the bundle of sheaths (C2b), and similarly, the bundle of needles (C1b). These habits form in a narrow temperature regime near −5 °C where growth is almost exclusively in the c-axis direction (e.g., Takahashi et al., 1991). However, unlike the needles, these crystal forms have widened significantly perpendicular to the c-axis. Such widening is hard to

reconcile with our knowledge of growth driven by layer nucleation, which may effectively shut off all normal growth of the prism faces. Two mechanisms may overcome this nucleation barrier. One is riming. A rimed drop on a prism plane may then sprout a new sheath protrusion along the c-axis. The second is sketched in Fig. 22c. In this mechanism, the protruding sheath widens as in the scroll form in (a), but overshoots the base crystal, thus advancing the crystal width perpendicular to the c-axis.

5　The protrusion will thicken, and may then develop a new prism face by the mechanism suggested for the scroll (Fig. 22a). In this way, a new sheath or needle can develop to the side of the original, producing a "bundle". Such overshooting of the prism planes in this case is analogous to the overshooting of the basal planes in the two-level crystal (§3.12).

3.20 Protruding growth on branch backsides and ridge pockets

The backsides of branches on tabular crystals appear to be largely non-crystallographic during growth under constant conditions.

10　But they are not gently curved; rather, various ridges and ribs are common, which show up as dark interior lines in images. However, when part of a relatively fast-growing crystal branch slows down, due to either a change of conditions or to the gradual drift toward the crystal interior as the outer parts grow out, the ridges and cross-ribs may form planar protrusions. For example, such protrusions appear relatively common on the slower-growing planar crystals in Takahashi (2014) at temperatures of −12.5 and −16.3 °C. Libbrecht (2006) refers to them as "aftergrowth plates", though they form while the crystal is growing. An

15　example is shown in Fig. 23a. Also, fairly common are long pockets that we call ridge pockets. Ridge pockets include the main-ridge pockets aligned towards the vertex and coming in a pair, as well as the side-ridge pockets aligned toward each side and generally having numerous pairs. Several examples appear in Fig. 23b. This image shows main-ridge pockets at A (enlarged inset upper left) and side-ridge pockets at B.
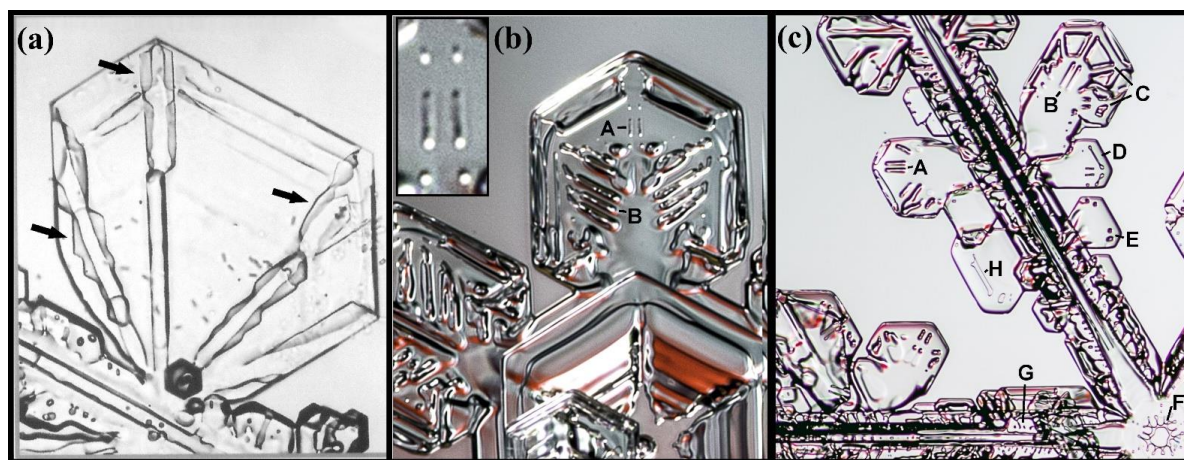

Figure 23: Protruding growth on branch backsides and branch pockets. (a) Sidebranch of dendrite. Arrows show protrusion features on ridges. (b) Branch of broad-branch crystal. Inset is close-up of main ridge pockets A on one branch, B marks side-ridge pockets. (c) Branch of dendrite. Sublimation has apparently exposed several pocket features A–H described in text. Image in (a) from large hoar crystal grown in an unforced air-flow cloud chamber of Yamashita and Ohno (1984). Crystals in (b) and
25　(c) from snow crystals collected at ground level (courtesy of Mark Cassino).

The dendrite branch in (c) shows numerous pocket features. (This crystal has undergone significant sublimation just before imaging, and thus most of the pockets appear to have re-opened. But it provides clear examples of pockets seen on other crystals.) Here, A and B mark main ridge pockets. C marks an example in which pockets can form where a main ridge meets a thickened cross-rib. At bottom is a pocket and at top is a position that may produce a pocket by such an intersection. D appears to

be an elongated edge pocket (§3.7). E and G appear to be side-ridge pockets, and F is a center ring pocket (not described here, but in Yamashita, 2018). Finally, H seems to be a center pocket. The main ridge pockets at B fade towards the main branch, indicating that the base of the pocket has a downward slope towards the tip. In images such as these, which show only one view, it is difficult to be sure that the features are pockets as opposed to channels or small hollows. Nevertheless, they appear to be

5   common and whether or not they are pockets or channels, their effect on scattering may be similar.

   The ridge pockets may form as sketched in Fig. 24. The branch backside often has a main ridge from the tip, shown in cross-section at (a). As pointed out by Frank (1982), the ridge produces a vapor-shadowing effect leading to the two parallel channels to both sides in the next sketch. These channels are clearly seen in images of most branched snow crystals and was noticed much earlier by Nakaya (1954). With a local growth slow-down, which may arise simply due to the branch tips growing further out,

10   thus depleting the crystal inner regions of vapor, lateral growth may start to dominate, creating the protruding growth in the next two sketches. This may continue and eventually close-off the channels making the two main ridge pockets at the bottom in (a). The mechanism for side-ridge pockets is sketched in (b). The process is like that of the main ridge, except side ridges can form close together, creating a central channel gap. Protrusion growth at the crest starts bridging the gap, and completes the pocket at the bottom. These sketches do not show the 3-D structure of the branch, in which the top surface slopes downward towards the

15   thinner outermost prism faces at the tip. Thus, the protrusions likely also grow from the interior region towards the tip (as in the corner-pocket case), eventually covering the entire backside.
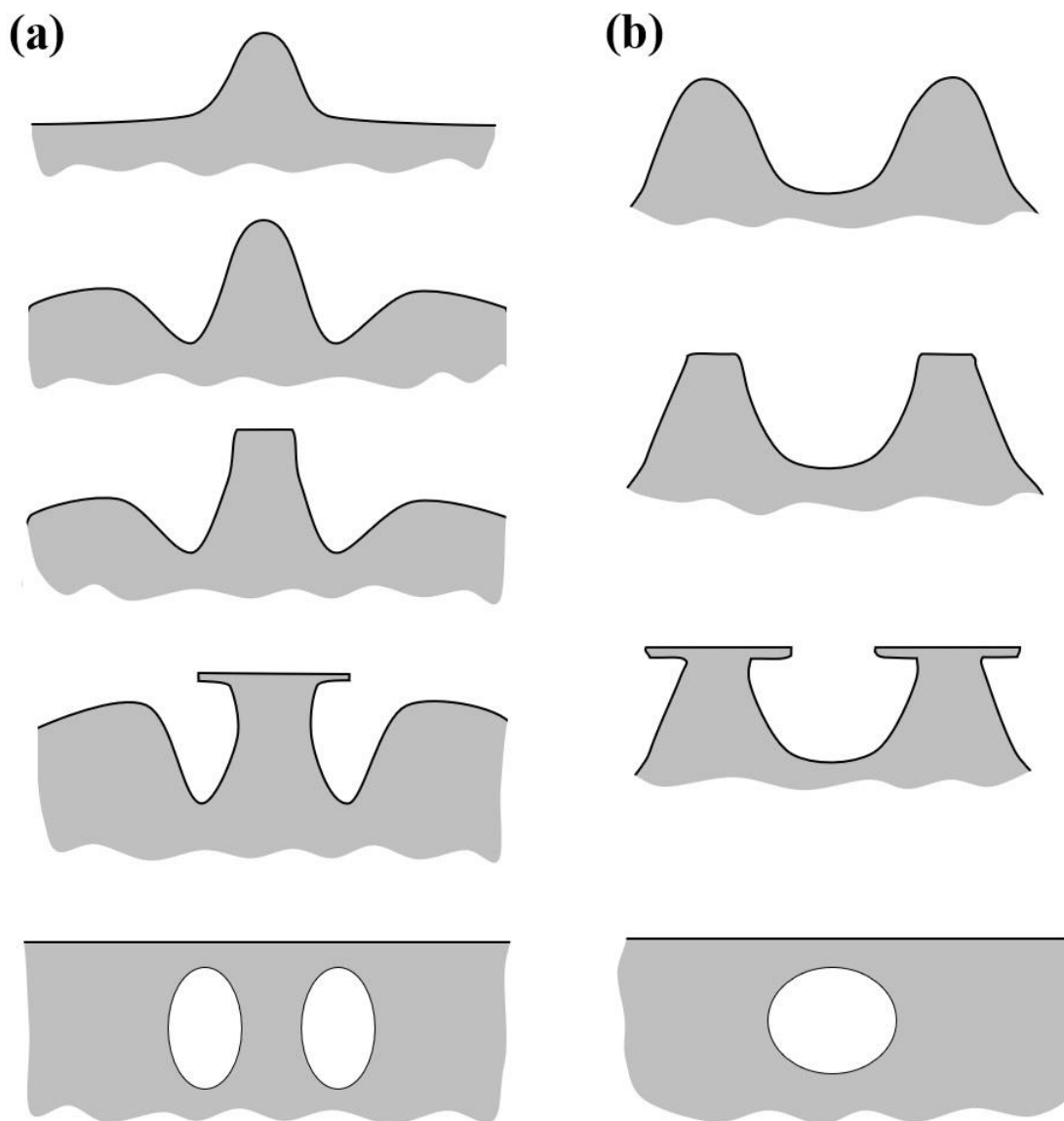
Figure 24: Development of ridge channel pockets. (a) Adjacent to main ridge. (b) Between side ridges.

3.21 AST contributions to trigonal formation and primary habit

5   Trigonal crystals have only three clearly observable prism faces, a striking feature that begs for an explanation. Another crystal
type with three-fold symmetry is the scalene hexagonal, which is shown together with the trigonal type in Fig. 24. Bentley
(1901) finds both types rare in precipitation, but Heymsfield (1986) reports on a very cold cloud in which roughly 50% of the
crystals had three-fold symmetry. In the laboratory, Yamashita (1973) found that numerous trigonal and scalene forms would
result from seeding with an adiabatic-expansion method to create sub-micron ice nuclei, but only hexagonal crystals would result

Atmospheric
Chemistry
and Physics
Discussions

from nucleating cloud droplets of much larger size. This finding may explain the difference in Bentley's and Heymsfield's findings because the latter observations were of crystals that likely formed on sub-micron droxtals. In Yamashita's sub-micron seeding experiments, the crystals grew at temperatures down to about −26 °C. The trigonal forms appeared stable when columnar; for example, about 10–20% of all crystals were trigonal in the columnar regime above −10 °C. But the trigonal tabular

5   forms appeared to transition to the scalene hexagonal at small sizes, with the latter types occurring in over 40% of the crystals at all temperatures except around −12 to −18 °C. In all cases the trigonal were more common than rhombohedral and pentagonal forms.
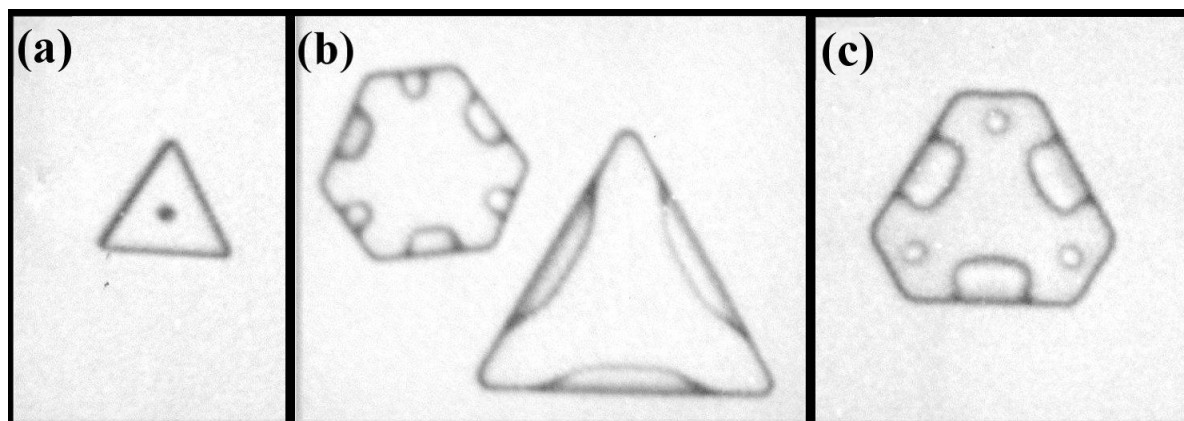

10 **Figure 25:** Trigonal and scalene hexagonal. (a) Trigonal. (b) Both types. (c) Scalene hexagonal. Crystals grown for about 310 s at −10.2 °C in the cloud chamber. Diameters are about 15–35 μm.

A recent review proposes three possible explanations for trigonal formation (Murray et al., 2015). In one, they suggest that stacking disorder can lead to growth of trigonal forms, but do not give a specific formation mechanism. Concerning a possible

15 mechanism, stacking faults in cubic crystals can produce trigonal forms (e.g., Millstone et al., 2009), but the mechanism involves alternating re-entrant corners that have not yet been shown to occur in stacking-disordered ice. Also, it is not clear how such a mechanism would explain Yamashita's observations above. Moreover, our observations here suggest that regions of stacking disorder may instead lead to near-symmetric hexagonal forms (e.g., Fig. 3). Thus, the stacking-disorder mechanism is both implausible and contrary to observations. Another explanation involves having equivalent dislocation step sources on just three

20 alternating prism faces. Such a mechanism cannot explain the preponderance of trigonal over rhombohedral and pentagonal forms. The third explanation involves aerodynamic factors (Libbrecht and Arnold, 2009). Such an explanation also appears inconsistent with Yamashita's findings above, specifically the greater stability of the columnar forms and the transition from trigonal to scalene hexagonal as the tabular forms grew larger. Instead of these proposed explanations, we suggest a closer look at the growth mechanism, focusing on two factors: a mechanism for their initial formation in sub-micron droxtals, and a

25 mechanism for their stability as they grow larger.
    A possible explanation for the formation of an initial trigonal habit from a sub-micron droxtal is sketched in Fig. 26a–d. When the sub-micron droplet freezes, one prismatic plane forms first. Assume, as in (b) that it is p_1 on the left side. If the crystal is smaller than x_s, lateral growth of the face may be dominated by AST yet increase in rate as the face expands. This rate would increase in proportion to the increase in area because all the vapor impinging on the area can migrate to the edge. Thus, lateral

30 growth would greatly favor the first face that develops. Moreover, this growth may overshoot, and effectively bury, the

Atmospheric
Chemistry
and Physics
Discussions

neighboring faces p_2 and p_6. If the next face that develops is either p_3 or p_5, then face p_4 would be similarly buried as shown in (c). As p_3 and p_5 expand, the crystal fills out as a trigonal form with only p_1, p_3, and p_5 faces as shown in (d). In this way, if after step (b), the three remaining faces were equally likely to form next, then the likelihood of a trigonal would be twice that of a crystal with four prism faces. Experimentally, the trigonals formed much more frequently than those of the rhombohedral and pentagonal (except at −4.2 °C), and thus the formation of the second prism face may depend on the formation of the first.
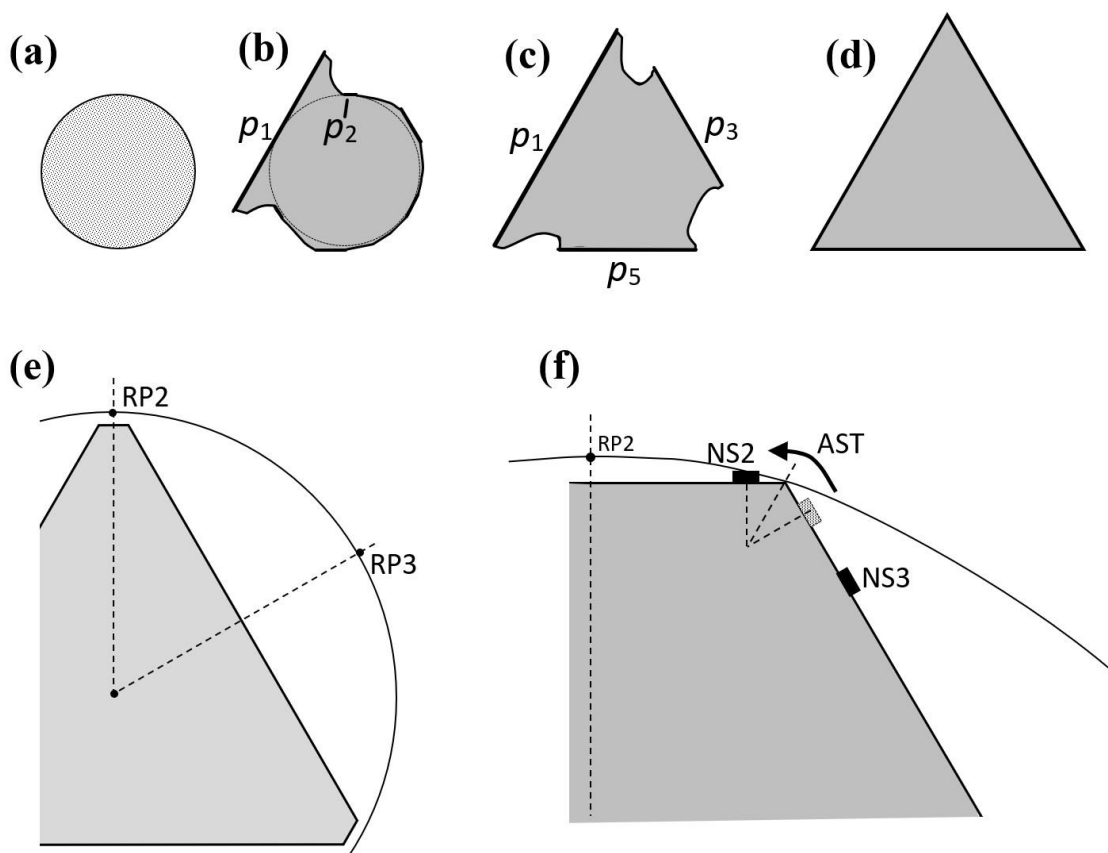

Figure 26: Formation and growth of a trigonal crystal. (a) Droplet before freezing. (b) Prism face p_1 forms before the others, growing via AST, stunting neighbors p_2 and p_6. (c) Prism face p_3 or p_5 develop next, also stunting p_4. (d) Trigonal forms. (e) Vapor density contour around nearly trigonal form (scalene hexagonal) with small prism faces. RP2 and RP3 are points on p_2 and p_3 where a reflection-symmetry plane crosses the contour. (f) Close up of corner between prisms p_2 and p_3. Solid boxes are the layer nucleation sites NS2,3. Shaded box on p_3 is the nucleation site in the absence of AST.

The trigonal form may then be maintained via an effect of the vapor-supersaturation contours on layer nucleation. The supersaturation contours around the crystal, viewed in the plane of Fig. 26e, should have the same symmetry as the crystal. In the sketch, the contour is a circle, but in general needs to only have reflection symmetry about the dashed lines from the center to points RP2 (reflection-symmetry point, face 2) and RP3 as shown. (Far from the crystal, the contour will be a circle, but closer to the surface, the lines will bend closer to the surface as suggested in (f). The consequence is the asymmetry in the contour about the vertex between p_2 and p_3, as shown. Assuming that the growth is via layer nucleation, with layer nucleation points near to, but not exactly at, the vertex, then such points on either side of the vertex will experience different vapor supersaturations. In

particular, point NS2 on face p_2 will have greater supersaturation and thus nucleate new layers at a faster rate than at the corresponding point on face p_3. This factor will increase the normal rate of growth of p_2 over that of p_3.

However, the rate of layer nucleation depends on the density of surface-mobile molecules, not the adjacent vapor density directly. Including this process will increase the difference between the two faces as follows. The faster production of new layers
5   at NS2 will draw a net AST flux from face p_3, thus reducing the surface ad-molecule concentration there. As a result, the layer nucleation point NS3 must move further away from the vertex, as shown in the sketch, further reducing the layer-nucleation rate on face p_3. In this way, the normal growth rate of p_2 can significantly exceed that of p_3 even with a relatively small vapor-density asymmetry, driving its area lower. The difference in growth rates between the faces may lead to the smaller face becoming relatively smaller or larger, depending on the ratio of the rates. (With a little trigonometry, you can readily work out the
10   condition for a relative decrease.) But if the face area shrinks, the effect here may increase, causing further shrinkage; conversely, if the face area grows, the effect may weaken, leading first to the scalene hexagonal and then to fully hexagonal. This AST effect on the relative layer nucleation rates between adjoining faces was previously proposed by Frank (1982) to explain the abruptness of primary-habit change with temperature. As he suggested, it should apply in general to the basal–prism edge as well, influencing the primary habits (aspect ratios) of snow crystals in general.

15   About the higher stability of columnar trigonal forms, consider the magnitude of the effect. The magnitude should depend on the size of the mean migration distance x_s on the prism faces compared to the crystal size. When the value of x_s is a significant fraction of the large-face diameter (e.g., 0.1 or more), the effect is likely to be stronger as NS3 is pushed further from the vertex. In contrast, when x_s is much smaller, then the shift of NS3 will be insignificant. The values of x_s are unknown, but Mason et al. (1963) argued that in the tabular regime, x_s should be relatively small (compared to the basal's value), but relatively large in the
20   columnar regime. Such a trend in x_s, if verified by experiment, could the explain the higher stability of trigonal columns as well as the transition to scalene hexagonal for the tabular case. The instability of the tabular case is also consistent with the argument that an imposed gradient in supersaturation has little effect on the direction of tabular branches (Nelson and Knight, 1998), that is, prism faces adjacent to a supersaturation maximum should grow at the same normal growth rate (unlike the case in Fig. 26f).

In addition, the AST flux from the basal to the prism should be smaller towards the narrow prism in a scalene hexagonal crystal
25   than to the wider prism (following §3.16). This effect would further de-stabilize the tabular trigonal and scalene hexagonal forms, particularly for the thinner tabular crystals, and have less effect on the columnar crystals. Concerning the role of the vapor mean-free path, this mechanism for the stability would have a vanishing role as the vapor mean-free path approached or exceeded the crystal size. But in an atmosphere of air, this would require crystal diameters below a few tenths of a micron. Finally, if the layer nucleation rate increased more rapidly at higher supersaturation, as is expected, then the influence of the AST
30   flux would increase as well, strengthening the mechanism. In general, the supersaturation in a cloud is higher when the first crystals nucleate, and is also higher at the crystal surface when the crystal is small, but as each crystal grows and more crystals nucleate, the supersaturation drops. This effect also predicts a transition from trigonal to scalene hexagonal, and eventually, to hexagonal. However, if the crystal develops branches while still scalene hexagonal, the nearly three-fold symmetry should remain as the branches grow independently of one another. This may explain the large, nearly three-fold symmetric branched
35   crystals in Bentley's collection (Bentley, 1924; Bentley and Humphreys, 1962).

Finally, consider what would result if, instead of p_3 or p_5 developing after p_1, that p_4 developed in Fig. 26c. In this case, one can argue that the resulting crystal would have two large-area prisms p_1 and p_4, with the latter smaller than the former, and just two other equal-sized faces p_3 and p_5. That is, the shape in cross-section would be an isosceles trapezoid. Such a shape falling with p_4 side down could generate the suncave Parry arc in a thin cloud. Upon growing larger, the p_2 and p_6 faces would likely develop,
40   and then regardless of whether the falling orientation had p_4 side down or up, a suncave Parry arc would result (e.g., Westbrook,

2011). A sampling of crystals from a Parry-arc display found no evidence of the trapezoid form (Sassen and Takano, 2000), so such a form may transition to the six-sided form while small.

3.22 Microscale mechanism of protruding growth

In considering the microscale mechanism of protruding growth, two obvious questions arise: (1) How does a thin protrusion
5   start? That is, instead of the AST molecules spreading out on the adjoining surface region to build-up a thick facet, why is the flux concentrated to a thin region? (2) Why would the thin front of the protrusion have a higher density of growth sites than the analogous facet to efficiently collect all the AST flux and continue protruding?

A possible answer to (1) is a large vapor-density gradient. Consider again the sketch in Fig. 1b. If the vapor-density contours closely parallel the surface, but "skim over" the inside corner **c**, then the vapor density would sharply decrease from **e** to **c**
10   provided that this distance exceeded the vapor mean-free path. In such a case, the AST flux may build up nearer to **e** and not reach **c**, initiating the protrusion analogous to forming an SCR during the hollowing process. Consistent with this argument is the observation that no cases of the corner pockets have been reported for small crystals and on crystals grown and sublimated in a pure vapor. Regardless, if one instead argues more generally that if we have a mechanism that answers (2), forming a high-density of growth sites in a thin region just over the edge of a facet, then a net flow of mobile surface molecules would not
15   migrate any further than this thin region. That is, the region would start protruding. Thus, it becomes even more important to find a possible mechanism that answers (2). A high-density of growth sites would exist if the front of the protrusion was rough. Such rough edges have been observed in numerous cases as discussed in §3.16. Thus, rough, thin protrusions may form and produce fast growth rates. However, it is not clear why only thin, and not also thick, protrusions would be rough.

A possible answer was proposed by Libbrecht (2003), who argued that thin plates must have a different structure at their
20   leading fronts that leads to a high deposition coefficient (i.e., a high density of growth sites such as a rough edge), and then suggested a type of nanoscale surface-melting effect. However, at nanometer sizes, the small radius of curvature may also increase the rate of sublimation, causing a compensating decrease in lateral growth rate. And though such a mechanism may help explain the fast-growing serrated dendrites at −2.0 °C and thin discs at slightly lower temperatures, it would be less likely at the much lower-temperature protruding-growth effects found here near −30.0 °C. Another possible answer is that the edge region
25   consists of rough, high-index planes that essentially vanish on larger surfaces due to their rapid growth but cannot vanish on a thin protrusion due to a curvature effect.

A simpler mechanism for fast protruding growth, and one more closely connected to an established theory, is layer-nucleation confined to a thin region on the protrusion front. There are several possible consequences of having a small thickness t (Fig. 19) that may promote nucleation. Based on such considerations, three mechanisms are briefly analyzed in Appendix B. The first two
30   mechanisms, which may work together, give possible ways that the nucleation of new layers on the edge will result in closer step spacings. The second of these, asymmetric nucleation from one basal–prism edge (Fig. 19b, middle) may be the most applicable to most cases considered here due to the likely strong supersaturation gradients involved. For extremely thin protrusions, the critical supersaturation itself may be lower, as argued in Appendix B for a third possible mechanism. Clearly, these mechanisms are currently speculative, but are mentioned here to spur more research of the topic. In particular, more experiments are needed
35   to understand the mechanism of protruding growth.

4 General implications

To test the general magnitude of the AST role in ice growth, lateral-growth measurements are needed with greater precision than those given here. An interferometry study may provide sufficient precision of the lateral-front height and contour of the perimeter. For deducing the resulting x_s values, the model introduced in Appendix A may be used. To test specific habit

5   mechanisms proposed here, we need better modeling—including vapor diffusion to realistic crystal shapes and relevant surface processes. Presently, the most realistic crystal-growth model is that of Wood et al. (2001), but it is limited to hexagonal prisms. Some approaches, such as cellular automata (Kelly and Boyer, 2014) and phase-field (Demange et al., 2017) model much more complex shapes, but they unfortunately do not appear to include any of the relevant surface microscale processes directly. The list of relevant surface processes includes layer nucleation, defect-step sources, step clumping, and non-crystallographic regions

10   (Nelson, 2005). To this list, we must now add that lateral-growth processes with AST must be included.

Concerning light scattering from atmospheric ice, some studies have suggested that the outermost ice-crystal faces can introduce "roughness" that affects the visible-light scattering (e.g., Voigtländer et al., 2018). But in the crystal-growth field, going back many decades, crystal faces are known to grow as atomically flat surfaces with nanoscale steps at low supersaturations, as occur in the atmosphere, except where hollows or branches sprout. Our experiments and observations are

15   consistent with this well-established view of growth. However, the interior regions such as backsides, hollows, and pockets can show bumpier structures, and these interior regions are the more likely source of the "roughness" implied by the scattering results. The pockets, however, cannot be detected using the oft-used method (e.g., in Smith et al., 2015) of examining ice-crystal replicas. In addition, for sublimation, our experiments showed no indication of rough features on the outermost surfaces (except the nanoscale roughness of a smoothly curved edge), such as those found in recent SEM studies (e.g., Magee et al., 2014;

20   Pfalzgraff et al., 2010). In those experiments, little air was present, thus differing from atmospheric ice crystals. The presence of air had been argued previously to be important for the observed smoothly rounded shapes of sublimating ice (Nelson, 1998).

5 Summary

We have described here some previously unreported features on vapor-grown ice, including corner pockets, elongated edge pockets, and planar pockets, as well as provided more detailed observations of hollow terracing and hollow close-off. We argued

25   that such features arose partly from lateral or protruding growth, both phenomena driven largely by surface transport across the boundary of a face to the advancing edge, a process we termed adjoining surface transport or AST. Several quantitative models have been introduced that apply to lateral growth, and several qualitative models have been presented linking lateral-type growth to known secondary habits.

Our central point is that such lateral and protruding growth, long neglected in ice and snow research, may help explain a wide

30   range of complex features and phenomena related to ice- and snow-crystal growth in the atmosphere, particularly when combined with normal growth. Protruding growth itself likely produces the two-level structure on stellar snow crystals and also helps to explain capped columns, multiple-capped columns, florid crystals, sheath growth, scrolls, sheath clusters, as well as various branch pockets and planar extensions. As argued here, lateral and protruding growth are also likely factors in hollow terracing, banding, and close-off to make center pockets. Finally, the AST process itself likely contributes to the growth rates of

35   sheath and dendritic crystals where it may substantially increase the growth rates and round-out the shape of the leading tip or corners. Finally, AST may also affect layer nucleation rates and explain trigonal forms.

As for immediate practical applications, we may infer the occurrence of an undersaturated cloud region via the observation of 12 corner pockets in a collected crystal, with the positions of the pockets providing the crystal size and aspect ratio at the time

Atmospheric
Chemistry
and Physics
Discussions

immediately after sublimation. However, such an interpretation requires care because corner pockets may also form whenever a change in growth conditions leads to a transition between rounded and facetted growth. Similar inferences of crystal conditions based on other crystal features will likely be revealed in subsequent experiments. Thus, gaining a greater understanding of the formation of hollows, pockets, and various thin protrusions may lead to more detailed knowledge of cloud conditions, and

5   conversely, lead to better predictions of their occurrence in models. In turn, the improved predictions may improve the modeling of radiative transfer through ice-containing clouds. With such widespread potential applications, the phenomenon of AST-driven lateral and protruding growth deserves greater study.

Appendix A: Modeling lateral and protruding growth

We introduce the three mechanisms for the lateral growth of a face for the fits in Fig. 5. Referring now to Fig. A1, assume r

10   marks the radial edge-front of the face with height h. The rate dr/dt is affected by I) direct vapor deposition to the edge-front, II) AST flux from the top basal face, from within x_s of r, and III) normal growth of the rough region laying between radial position r and the radius a of the crystal. Cases I and II involve a face edge-front of height h, whereas h is assumed zero for III. In case III, the position r is the intersection of the curved face and the basal-face position $z = c$, marked with a dot in the sketch.
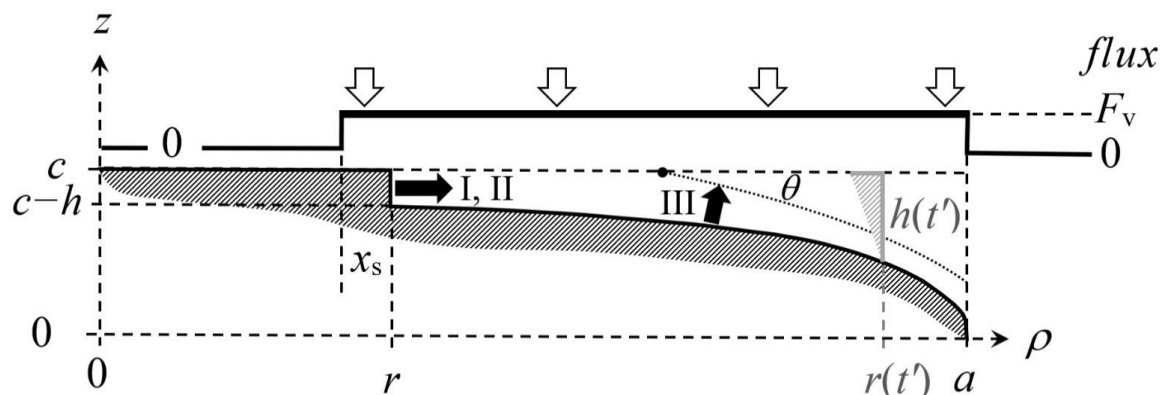

Figure A1: Lateral growth models. Dark shading shows the surface region of one quadrant of the crystal cross-section at a given time t. The flux calculation treats the crystal as a thin disc of radius a with flux F_v uniform between $r-x_s$ and a, zero elsewhere (upper plot). The face edge-front at radial position r has height h for mechanisms I and II. At a later time t', the value of h is larger (light shading) due to the advancement to $r(t')$, making a larger distance between the rough surface and basal surface at c.
20   For III, the edge-front is instead assumed to lie at the intersection of the laterally growing face at c (dashed line) and the dotted curve.

All three mechanisms for dr/dt depend on the vapor flux to the face, so we first estimate this flux. Assuming zero normal growth of the face (the basal face in this case), the flux normal to the face must be zero out to within x_s of the face-edge at r.
25   Beyond this point we assume a uniform flux F_v (#/m²s) in the z direction out to the edge of the crystal and then zero beyond. For the flux calculation, the crystal is assumed to be an infinitesimally thin disc of radius a. As done for other uniform-flux calculations (e.g., Nelson and Baker, 1996), the value of F_v is determined self-consistently through an assumed surface response (deposition-coefficient function) to the vapor density at the surface, with the vapor density depending on F_v. The rates for I–III, top-to-bottom are

Atmospheric
Chemistry
and Physics
Discussions

$$\frac{dr}{dt} = \Omega F_v \frac{x_s}{h}\left(1 - \frac{x_s}{2r}\right) \quad , \qquad \begin{matrix} \Omega F_v \\ \\ \Omega F_v \frac{1}{\sin(\theta)} \end{matrix}$$

A1

where Ω is the volume occupied by a water molecule in ice (mass of molecule/mass-density), and θ is the angle between the rough surface beyond r and the basal face. To calculate this angle, we assume that this rough surface is the perimeter of an expanding ellipsoid of the same, fixed aspect ratio of the crystal. Such an assumption is unlikely to be accurate in detail, but

5 nevertheless includes the influence of an increasing angle θ as the face grows laterally. For the calculations, we followed the treatment of the ellipsoidal coordinate system in Moon and Spencer (1961), and do not give the details here. For cases I and III, the flux is assumed to be normal to the surfaces (edge h and rough region, respectively) in A1, even though the flux is assumed as along the z-axis for the calculation of F_v. For case II, the value of h is not known from the measurements, and thus is treated as a fitting parameter here and then compared with the initial crystal profile. It only remains to determine F_v.

10 In a stagnant atmosphere of air, the vapor density N surrounding a thin disc of radius a has flux $D\partial N/\partial z$ at the surface. For the first step of the calculation, we assume this flux is uniform over the entire top surface (i.e., $0 \le \rho \le a$). Shifting and normalizing as

$$\begin{aligned} \Delta N' &\equiv \frac{N(\rho',z')-N_\infty}{N_\infty} \\ F_v' &\equiv \frac{\partial \Delta N'}{\partial z'} \\ \rho' &\equiv \frac{\rho}{a} \\ z' &\equiv \frac{z}{a} \end{aligned} \quad ,$$

A2

with N_∞ the far-field vapor density, the solution for uniform F_v' can be shown to equal

15 $\Delta N'(\rho',z') = -F_v' \cdot h_{td}(\rho',z')$,

A3

where the thin-disc basis function h_{td} is an integral of Bessel functions (Nelson, 1994). (This function is defined the same in A3 as are the analogous basis functions h for the cylinder (Nelson and Baker, 1996; Nelson, 2001) and Q for the hexagonal prism (Wood et al., 2001).) At the surface ($z' = 0$), this function simplifies to

$$h_{td}(\rho',0) \equiv \begin{cases} {}_2F_1\left(\frac{1}{2}, -\frac{1}{2}, 1, \rho'^2\right) & \rho' \le 1 \\ \frac{2}{\pi}E(\rho'^2) & \rho' > 1 \end{cases} \quad ,$$

A4

20 where $_2F_1$ is the hypergeometric function and E the elliptic integral. The curve is roughly bell-shaped about the origin, where it equals one, then nearly equaling $1/2\rho'$ for $\rho' > 1.5$. Consider now the "thin-ring" basis function h_{tr} defined as

$h_{tr}(\rho',z',r',x'_s) \equiv h_{td}(\rho',z') - \frac{1}{\gamma}h_{td}(\rho'\gamma, z'\gamma)$,

A5

where

$\gamma \equiv \frac{a}{r-x_s} \equiv \frac{1}{r'-x'_s}$,

A6

25 always exceeds one. You can readily show that the derivative of this function normal to the surface ($\partial/\partial z'$) gives a non-zero value at the surface only in the ring $r-x_s \le \rho \le a$ (or $1/\gamma \le \rho' \le 1$), where the value equals -1. For the edge-front, the relevant part of the function lies at $\rho = r$. We plot h_{tr} at this position in Fig. A2.
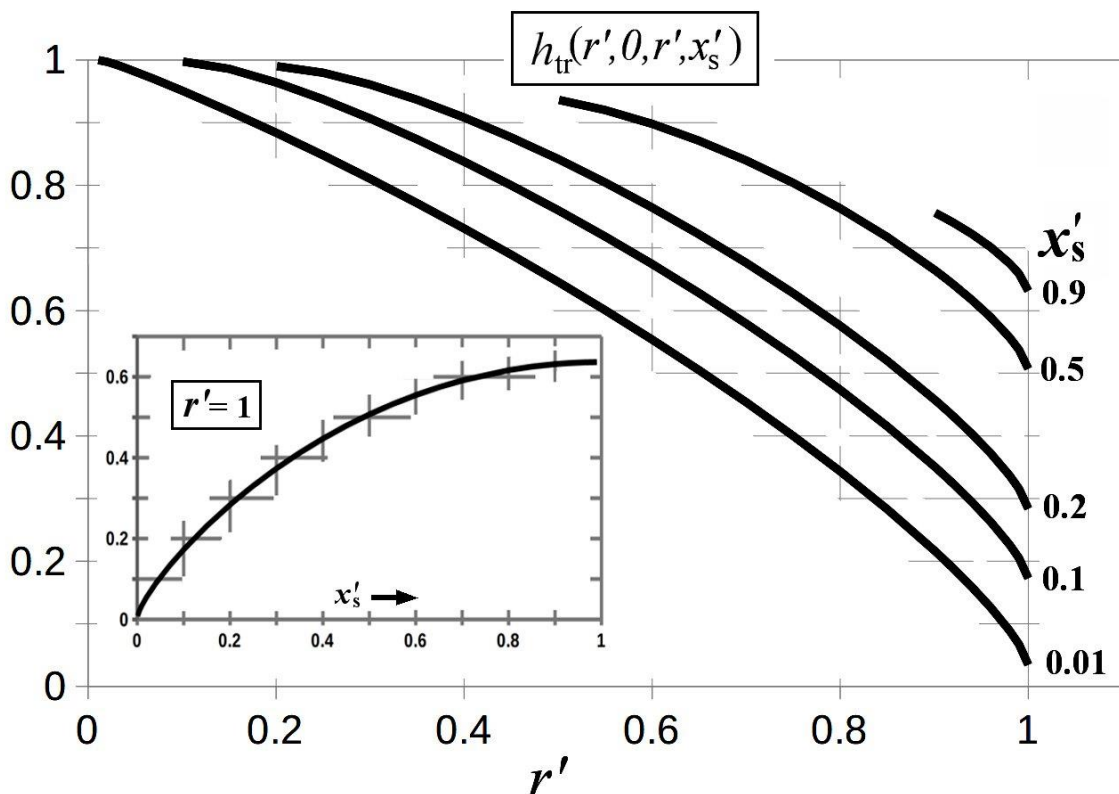
Atmospheric
Chemistry
and Physics
Discussions

Open Access

EGU

Figure A2: Basis function h_{tr} for the thin ring. The function is evaluated at $z' = 0$ (i.e., the surface) and ρ' at the position of the growing face edge-front (r'). The five curves are for the x'_s values given at right. Inset plot shows the dependence on x'_s when the edge-front reaches the crystal perimeter at a (i.e., $r' = 1$). Hatches show the grid.

5

As the face edge-front r' moves towards the crystal perimeter, the area that collects vapor decreases. This behavior is reflected in the decrease in h_{tr} as $r' \rightarrow 1$ for all values of x_s. Each curve for a given x'_s value begins at $r' = x'_s$ because the vapor-collection region starts at $r' - x'_s$, which cannot be negative. And when this starting point at x'_s increases, the function decreases because h_{td} decreases away from the origin. Exactly at the rim, where $r' = 1$, the only region of vapor collection is the ring of width x'_s (Fig. A1). Thus, in this case, h_{tr} approaches zero as $x'_s \rightarrow 0$, as shown in the inset plot; that is, a thin ring of growth hardly depletes the surrounding vapor.

Calculating the flux requires the surface-kinetic expression for the flux. Assuming a rough surface, the flux at the edge-front is one-fourth the vapor mean speed v times $N(r',0) - N_{eq}$ (see, e.g., Nelson and Baker, 1996), which can be rewritten as

$$F'_v = a'(\Delta N'(r',0) - \tfrac{N_{eq}}{N_\infty}\sigma_\infty) \quad , \tag{A7}$$

where $a' \equiv va/4D$ is approximately the crystal radius divided by the vapor mean-free-path. From Eqs. A3 and A7, one can eliminate $\Delta N'$ to derive

$$F_v = \frac{\frac{v}{4}N_{eq}\sigma_\infty}{1 + a'h_{tr}(r')} \quad , \tag{A8}$$

Atmospheric
Chemistry
and Physics
Discussions

where $h_{tr}(r')$ is shorthand for the full expression plotted in Fig. A2. This expression is used with Eqs. A1 to plot the curves in Fig. 5.

The method of linear superposition of basis functions, as shown in Eq. A5, can be extended by adding more terms to properly treat the case of rough growth in the region $r-x_s \leq \rho \leq a$. That is, instead of a single ring of uniform flux with deposition

5 coefficient unity, one can break the ring into many smaller rings, and then sum the terms. Nevertheless, the treatment here should capture the essential features of the diffusion field $\Delta N'$.

For protruding growth, the behavior of h_{tr} for $r' = 1$ (inset, Fig. A2) is relevant. For example, having $x_s = 5$ μm with a face radius $a = 100$ μm gives h_{tr} of only ~ 0.08. Moreover, this value will decrease further as the protrusion grows due to a increasing at fixed x_s. Having such low vapor depletion will not only speed up the lateral growth, but may also allow the protrusion to

10 nucleate layers more closely, possibly aiding a roughening transition as discussed in Appendix B. Of course, this treatment assumes no normal growth of the face and no direct vapor flux to the edge in the radial direction. Such modifications can be added. The resulting expression will be similar in form to Eq. A8, but with added terms in the denominator.

Appendix B: Nucleation on a thin-edge face

As argued by Frank (1982), nucleation of layers on snow crystals differs from the classical multinucleation treatment (e.g.,

15 Arima and Irisawa, 1990) due to the lateral supersaturation gradients on a face. Specifically, the new layers will repeatedly nucleate at the spot of highest supersaturation. In addition, the nucleation of a layer can locally reduce the surface ad-molecule supersaturation, meaning that a new layer will not nucleate until the step-edge of the previously nucleated layer moves a certain distance l. This l will be approximately the distance from the step-edge, where the surface supersaturation is relatively low, to the point where the surface supersaturation reaches the critical value σ_{cr} to nucleate the next layer. This process is described in

20 Nelson (2001, Appendix A) for the case of nucleation on a wide terrace (step-free facet region). The purpose here is to examine how this process may differ on a thin-edge face, particularly in regards to reduced step-spacings and effectively rough growth.

For comparison, first consider the 1-d case in cartesian coordinates. Here the BCF equation (Burton et al., 1951) can be written

$$\frac{d^2\sigma}{dx'^2} = \sigma - \sigma_s \quad , \tag{B1}$$

where σ is the surface supersaturation of ad-molecules, σ_s is the value far from a step (where it becomes equal to the vapor

25 supersaturation adjacent to the surface), and x' is the distance from the step-edge normalized by the mean migration distance x_s. If the ad-molecules approaching the step edge from above (the upper terrace) encounter no barrier, and if the step edge is rough, then the boundary condition would be the equilibrium value, meaning $\sigma = 0$ there. But in general, there may be some barrier from above with $\sigma = \sigma_a$ there. (For nucleation on the upper terrace, the boundary condition at a lower-terrace step-edge does not matter.) For this general case, the solution is

30 $$\sigma - \sigma_s = (\sigma_a - \sigma_s)e^{-x'} \quad . \tag{B2}$$

With this solution, the normalized distance $l' = l/x_s$ as defined above is found by setting $\sigma = \sigma_{cr}$:

$$l' = \ln\left(\frac{1-\sigma_a{}'}{1-\sigma_{cr}{}'}\right) , \tag{B3}$$

where $\sigma_{cr}{}' = \sigma_{cr}/\sigma_s$ and $\sigma_a{}' = \sigma_a/\sigma_s$. This result shows that as $\sigma_{cr}{}' \to 1$, $l' \to \infty$ as expected, meaning that the crystal face stops growing and becomes perfectly flat. Our interest is in the opposite situation: specifically, the decrease in l' for $\sigma_{cr}{}' < 1$. Where l'

35 << 1, the deposition coefficient becomes unity, and the face region is effectively rough.

The case of a thin-edge face may involve a relatively short step of length nearly the face thickness t as shown in Fig. 19b (bottom), with the step-edge drawing surface ad-molecules via AST from the adjoining faces. Thus, the ad-molecules diffuse from two dimensions to the step, instead of just one for the wide-terrace case. For simplicity, we assume that x_s is the same on both face types and the short step is approximated by a closed-curve step of the same total length as shown in the sketch. Also,

5 consider only the case with $\sigma_a = 0$. With these simplifications, the problem becomes the same as the previous, except Eq. B1 becomes the analog equation for the radial coordinate in two dimensions. The solution is

$$\sigma = \sigma_s \left(1 - \frac{K_0(r')}{K_0(r_0')}\right) \ , \qquad\qquad\qquad\qquad B4$$

where r_0' is the normalized radius of the step having same length as the face width ($= t/2\pi x_s$) and K_0 is the modified Bessel function of the second kind of order 0. In general, K_0 falls off with distance faster than the exponential (Eq. B2) to express the

10 physical situation in which the step is contained in a small region, unlike the infinite step of the wide-terrace case. But in this case, solving for $\sigma = \sigma_{cr}$ to find the corresponding step-spacing l'_{AST} must be done numerically. (For l'_{AST}, the solution r_{AST}' is subtracted by r_0' to get the distance to the previous step edge.) We found the solutions for a range of normalized face-thicknesses t/x_s and supersaturations σ_{cr}/σ_s and show them in Fig. B1.
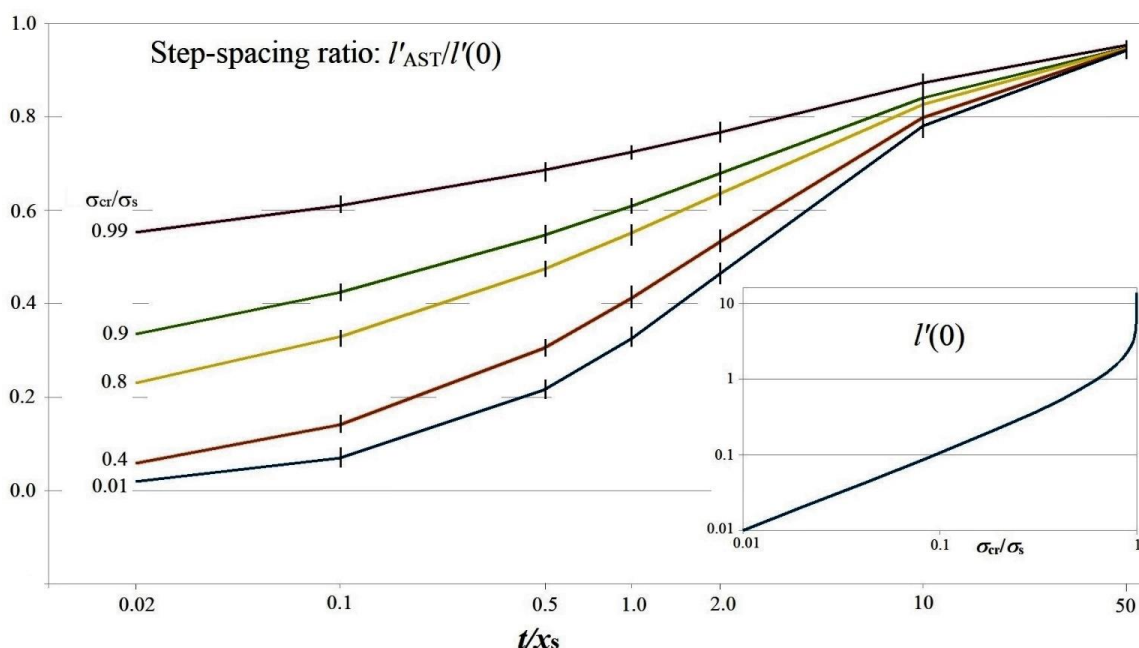

Figure B1: Ratio of calculated step spacing for a thin edge (from Eq. B4) to that for a wide terrace (Eq. B3) for $\sigma_a' = 0$. Inset shows the normalized spacing l' (Eq. B3). The crystal thicknesses t/x_s are marked on the abscissa label and the normalized critical supersaturations for each curve is labeled on the left side. Curve endpoints and inflection points are the calculated points.

20 The results show that the steps should always be closer on the thin-edge face, more so for thinner faces t and for smaller critical supersaturations σ_{cr}. Thus, at a given σ_{cr}/σ_s, the thinner the crystal, the closer the steps. The steps may even become close enough to effectively roughen the face, leading to a rounded form. For example, at $\sigma_{cr}/\sigma_s = 0.8$, thinning from t/x_s from 2.0 to 0.5

Atmospheric
Chemistry
and Physics
Discussions

decreases the step-spacing by about 30%. Being a relatively small amount, a rough–facet transition by this process might not be abrupt, and thus may not be the key factor in the observed roughening of thin crystals and protrusions.

The inset to Fig. B1 shows that unless $\sigma_s \gg \sigma_{cr}$, the step spacing remains relatively large; for example, even when $\sigma_s = 10\sigma_{cr}$, the spacing is just $x_s/10$. Given that x_s is very large on the molecular scale, this spacing might not appear sufficient for observed

5 rounding. (And in general, for growth in an atmosphere of air, σ_s is likely to remain just a little below σ_{cr}). However, several factors can reduce this step spacing. Consider first that very close steps become possible when σ_a' approaches 1 according to Eq. B3. A value of 1 would imply complete reflection at the top edge, and thus completely turn off AST, which we have argued does not happen. But intermediate values may occur that allow both appreciable AST and closer steps. To estimate how these intermediate values would affect l', we plot Eq. B3 for σ_a' from 0 to 1 and four values of σ_{cr}' in Fig. B2.
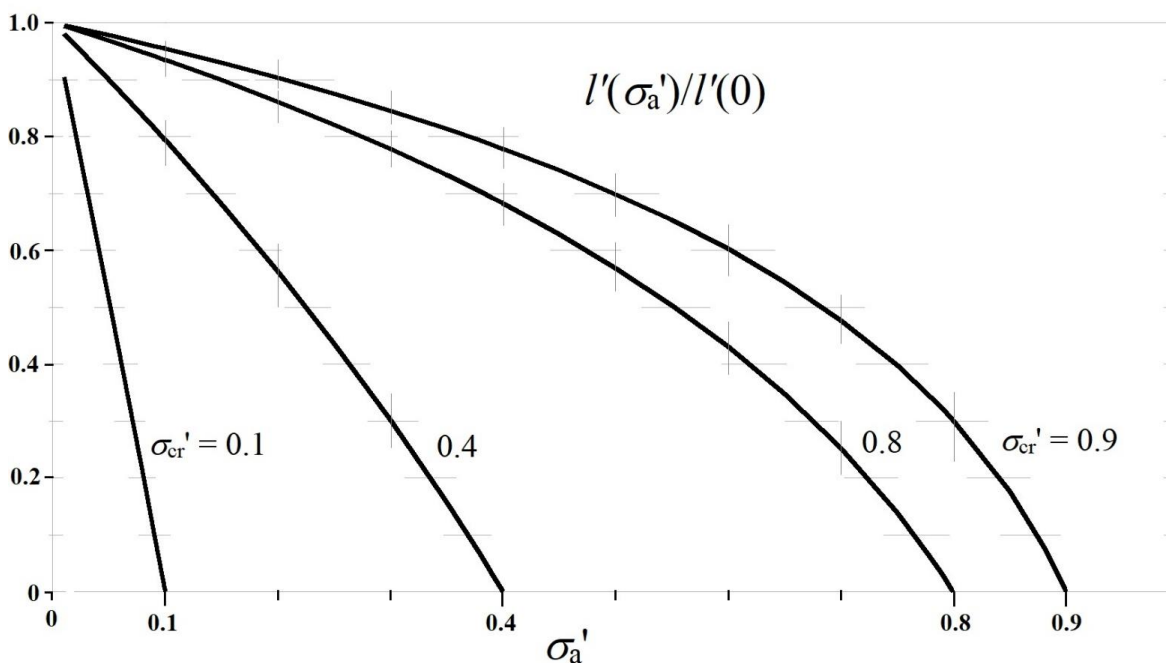
10

Figure B2: Normalized step spacing from nucleation for the case with non-zero boundary-condition at top edge of step. Four critical supersaturation values are marked on separate curves.

15 The curves show a sharp decrease in step spacing with increasing boundary-condition factor σ_a', particularly near σ_{cr}'. Thus, for sharp rounding near the layer-nucleation point, a relatively high value of σ_a' may be needed. Presently, we have no estimate of its value or an argument for whether or not σ_a' may be larger for the thin-edge situation. Also, the treatment here does not consider the nucleation-rate itself and its area dependence (as in Nelson, 2001), but this simplified treatment has allowed us to more easily see the trends with t and σ_a'.

20 Another factor that may effectively roughen a thin face involves vapor-density asymmetry. That is, one of the basal–prism edges should have a slightly higher vapor supersaturation than the other, leading to nucleation occurring at this edge. Say, as in the sketch in Fig. 19b (middle), this is the top edge. Moreover, due to either edge-energy considerations or the supersaturation gradient, the new layer spreads out along the edge first, and then, as a nearly straight step, moves down to the bottom edge. Once

reaching the bottom edge, it ceases to be a molecular sink of ad-molecules, splitting into a step going left and one going right, separated by some distance greater than t, say $n*t$, $n > 1$. The surface density of ad-molecules rises to the value needed to create the next layer, and the process repeats, with the steps splitting off quickly closing in on the previously nucleated steps. If one views the steps as fragments of concentric rings, their common center on the top basal face, one can see that at some distance

5   from **e**, their separation l should be close to their separation at **e**, that is, t, but travelling along the edge instead of across it. Thus, even when σ_s is just slightly below σ_{cr}, the step spacing near **e** can be roughly t, which can be much less than x_s. In this case, l is much more sensitive to t than the AST effect considered in Fig. B1: instead of changing by 30% when t/x_s changes from 2.0 to 0.5, l would decrease by a factor of 4.

For rounding to occur, the steps initially need only be slightly less than x_s. Rounding can occur because when $l < x_s$, the steps

10   respond to the local effective supersaturation, closing in together where this supersaturation is lower. That is, the normal growth rate at a point on the surface becomes proportional to the local effective supersaturation, thus decreasing where this supersaturation is lower. When this occurs near the tip, the tip rounds. Finally, for sufficiently high σ_s, the steps may even clump before reaching the opposite basal edge, in which case the new edge becomes the position of the step-clumping region (SCR), thus reducing the value of t. Thus, this asymmetry may lead to thinner faces. A similar argument appears in Nelson (2005) for

15   the changing thickness of dendritic branch tips with changing growth conditions.

The layer-nucleation process itself may be affected by the face thickness t for sufficiently small t. For example, to nucleate a new layer, the radius of a growing embryo must reach a critical size r_c to continue growing and become a new layer. This size depends on the step-edge energy κ, and the ad-molecule supersaturation. But on the thin-edge face, this embryo may need to grow only a value of $t/2$ before intersecting the face-edges and thereafter its edge may quickly adjust and straighten into two

20   straight steps, thus surmounting the edge-energy barrier. The following crude estimate of this effect is based on Appendix A of Nelson (2001). Consider the critical radius size at the critical supersaturation:

$$r_c = \frac{a_0 \kappa}{k_B T \sigma_{cr}} , \qquad\qquad\qquad B5$$

where $a_0 = 8.85 \times 10^{-20}$ m is the approximate ad-molecule area on the surface, k_B is Boltzmann's constant, and T is the temperature. The critical supersaturation is defined as that at which one embryo per second reaches this critical value, then

25   growing into a new layer. In the estimate here, the embryo only needs to reach $t/2$, which, when substituted into Eq. B5, gives us an effective edge energy κ_e. The resulting effective critical supersaturation for the thin-edge face is based on the expression for σ_{cr} found in Nelson (2001):

$$\sigma_{cr-e} = \frac{\pi a_0 \kappa_e^2}{48 (k_B T)^2} . \qquad\qquad\qquad B6$$

When the prism-face critical supersaturation of 0.4% (Nelson and Knight, 1998) is used in Eq. B5 to estimate κ_e and the value of

30   a_0 inserted, the resulting expression gives $\sigma_{cr-e} \approx 3t^2$, when t is expressed in micrometers. Thus, the effective critical supersaturation becomes smaller than the wide-terrace value when t become less than about 0.04 μm. Given the crudity of the model, these values are certainly not quantitively accurate, but they do suggest a sensitive dependence on crystal thickness when the crystal or protrusion is very thin. If the estimate of ~ 0.04 μm is accurate within an order-of-magnitude, then this effect cannot explain the observed rounding on the thin-disc crystals (thickness ~ 5 μm), but it may be a factor in the thin protrusions

35   during corner-pocket formation and the thin tips of needles and rounded dendrites. However, for such thin protrusions, the curvature of the overall protrusion itself would also have a limiting effect via the increase in equilibrium vapor density near the edge.

Atmospheric
Chemistry
and Physics
Discussions

Atmospheric
Chemistry
and Physics
Discussions

Open Access

EGU

References

Arima, Y. and Irisawa, T.: The back-force effect in the multinucleation growth process. J. Cryst. Gr., 104, 297−309, 1990.

Asakawa, H., Sazaki, G., Yokoyama, E., Nagashima, K., Nakatsubo, S., and Furukawa, Y.: Roles of Surface/Volume Diffusion
5 in the Growth Kinetics of Elementary Spiral Steps on Ice Basal Faces Grown from Water Vapor. Cryst. Growth Des. 14, 3210−3220. dx.doi.org/10.1021/cg4014653, 2014.

Avramov, I.: Kinetics of growth of nanowhiskers (nanowires and nanotubes). Nanoscale Res Lett., 2, 235–239, doi 10.1007/s11671-007-9054-8, 2007.

Bacon, N. J., Baker, M. B., and Swanson, B. D.: Initial stages in the morphological evolution of vapour-grown ice crystals: A
10 laboratory investigation. Q. J. R. Meteorol. Soc., 129, 1903–1927, 2003.

Bentley, W. A.: Twenty years' study of snow crystals. Monthly Weather Rev. May, 212–214, 1901.

Bentley, W. A.: Forty years' study of snow crystals. Monthly Weather Rev. Nov., 530–532, 1924.

Bentley, W. A. and Humphreys, W. J.: Snow Crystals. Dover Publications, 226 pp., 1962.

Burton, W. K., Cabrera, N., and Frank, F. C.: The Growth of Crystals and the Equilibrium Structure of their Surfaces. Phil. Trans. R.
15 Soc. A , 243, 299–358, 1951.

Demange, G., Zapolsky, H., Patte, R., Brunel, M.: Growth kinetics and morphology of snowflakes in supersaturated atmosphere using a three-dimensional phase-field model. Phys. Rev. E, 96, 022803 (1–13), 2017.

Frank, F. C.: Japanese work on snow crystals. J. Cryst. Growth, 24/25, 3–5, 1974.

Frank, F. C.: Snow Crystals. Contemp. Phys., 3–22, 1982.

20 Elwenspoek, M. and van der Eerden, J. P.: Kinetic roughening and step free energy in the solid-on-solid model and on naphthalene crystals. J. Phys. A: Math. Gen. 20, 669-678, 1987.

Fukuta, N. and Takahashi, T.: The Growth of Atmospheric Ice Crystals: A Summary of Findings in Vertical Supercooled Cloud Tunnel Studies. J. Atmos. Sci., 56, 1963–1979, 1999.

Gonda, T. and Gomi, H.: Morphological instability of polyhedral ice crystals growing in air at low temperature. Annals of
25 Glaciology, 6, 222−224, 1985.

Gonda, T. and Koike, T.: Growth mechanisms of single ice crystals growing at a low temperature and their morphological stability. J. Cryst. Gr., 65, 36−42, 1983.

Gonda, T. and Nakahara, H.: Formation mechanism of side branches of dendritic ice crystals grown from vapor. J. Cryst. Gr., 160, 162−166, 1996.

30 Gonda, T., Sei, T., and Gomi, H.: Surface micromorphology of columnar ice crystals growing in air at high and low supersaturations. Mem. Natl. Inst. Polar Res., Special issue, 39, 108–116, 1985.

Gonda, T., and Yamazaki, T.: Morphology of ice droxtals grown from supercooled water droplets. J. Cryst. Gr., 45, 66−69, 1978.

Gonda, T., and Yamazaki, T.: Initial Growth forms of Snow Crystals Growing from Frozen Cloud Droplets. J. Meteor. Soc. Jpn., 62, 190−192, 1984.

35 Hallett, J.: The growth of ice crystals on freshly cleaved covellite surfaces. Philos. Mag. 6 (69), 1073−1087, 1961.

Heymsfield, A. J.: Ice Particles Observed in a Cirriform Cloud at −83 °C and Implications for Polar Stratospheric Clouds. J. Atmos. Sci. 43, 851–855, 1986.

Atmospheric
Chemistry
and Physics
Discussions

Higuchi, K., Fushimi, H, Nishimura, Y., Sanda, E., Takahashi, Y., Kanda, K., Sumikawa, S., and Shimabayashi, S.: Growth of large frost crystals in cold chamber. Seppyou (Journal of the Japanese Society of Snow and Ice), 73 (Sept. Issue), 347–357, 2011. (In Japanese)

Hudait, A., and Molinero, V.: What Determines the Ice Polymorph in Clouds? J. Amer. Chem. Soc., 138, 8958–8967, 2016.

5   DOI: 10.1021/jacs.6b05227.

Itoo, K.: Forms of Ice Crystals in the Air: On Small Ice Crystals (II). Papers in Meteorology and Geophysics, 3, 207–216, 1953.

Järvinen, E., Jourdan, O., Neubauer, D., Yao, B., Liu, C., Andreae, M. O., Lohmann, U., Wendisch, M., McFarquhar, G. M., Leisner, T., Schnaiter, M.: Additional Global Climate Cooling by Clouds due to Ice Crystal Complexity. Atmos. Chem. Phys. Discuss., https://doi.org/10.5194/acp-2018–491, 2018.

10   Keller, V. W., McKnight, C. V., and Hallett, J.: Growth of ice discs from the vapor and the mechanism of habit change of ice crystals. J. Cryst. Gr. 49, 458–464, 1980.

Kelly, J. G., Boyer, E. C.: Physical Improvements to a Mesoscopic Cellular Automaton Model for Three-Dimensional Snow Crystal Growth. Cryst. Growth Des., 14, 1392–1405, 2014.

Kikuchi, K., Kameda, T., Higuchi, K., and Yamashita, A.: A global classification of snow crystals, ice crystals, and solid

15   precipitation based on observations from middle latitudes to polar regions. Atmos. Res., 132-133, 460–472, 2013.

Knight, C. A.: Ice Growth from the Vapor at −5 °C, J. Atmos. Sci., 69, 2031–2040, 2012.

Knight, C. A. and Devries, A. L.: Growth forms of large frost crystals in the Antarctic. Journal of Glaciology, 31, 127-135, 1985.

Kobayashi, T.: On the Variation of Ice Crystal Habit with Temperature. Physics of Snow and Ice. Proceedings, Institute of Low Temperature Science, Hokkaido University: Sapporo, 95−104, 1967.

20   Kobayashi, T., Furukawa, Y., Kikuchi, K., and Uyeda, H.: On twinned structures in snow crystals. J. Cryst. Gr., 32, 233–249, 1976.

Kobayashi, T., and Ohtake, T.: Hexagonal Twin Prisms of Ice. J. Atmos. Sci. 31, 1377–1383, 1974.

Kuroda, T., Irisawa, T., and Ookawa, A.: Growth of a polyhedral crystal from solution and its morphological stability. J. Cryst. Gr., 42, 41–46, doi: 10.1016/0022-0248(77)90176-2, 1977.

25   Libbrecht, K. G.: Explaining the formation of thin ice crystal plates with structure-dependent attachment kinetics. J. Cryst. Gr., 258, 168–175, 2003.

Libbrecht, K. G.: The physics of snow crystals. Rep. Prog. Phys. 68, 855–895, 2005.

Libbrecht, K. G.: Field Guide to Snowflakes. Voyageur Press, Minneapolis, MN, 112 pps, 2006.

Libbrecht, K. and Arnold, H. M.: Aerodynamic stability and the growth of triangular snow crystals. arXiv:0911.4267

30   (http://arxiv.org/abs/0911.4267), 2009.

Magee, N. B., Miller, A., Amaral, M., Cumiskey, A.: Mesoscopic surface roughness of ice crystals pervasive across a wide range of ice crystal conditions. Atmos. Chem. Phys. 14, 12357–12371, doi:10.5194/acp-14-12357-2014, 2014.

Maeno, N. and Kuroiwa, D.: Gas Enclosures in Snow Crystals. Low Temperature Science, Ser. A, 24, 81–89, 1966. (in Japanese)

Magono, C. and Lee, C. W.: Meteorological Classification of Natural Snow Crystals. J. Faculty of Science, Hokkaido Univ. Ser.

35   7, Geophysics, 2(4), 321–335, 1966.

Malkin, T. L., Murray, B. J., Brukhno, A. V., Anwar, J., and Salzmann, C. G.: Structure of ice crystallized from supercooled water. Proc. Nat. Acad. Sci., 109, 1041–1045, 2012.

Mason, B. J., Bryant, G. W., and van den Heuvel, A. P.: The growth habits and surface structure of ice crystals, Philos. Mag., 8, 505–526, 1963.

Millstone, J. E., Hurst, S. J., Métraux, G. S., Cutler, J. I. and Mirkin, C. A.: Colloidal gold and silver triangular nanoprisms. Small, 5, 646–664, 2009.

Ming, N-b., Tsukamoto, K., Sunagawa, I., and Chernov, A. A.: Stacking faults as self-perpetuating step sources, J. Cryst. Gr., 91, 11–19, 1988.

5 Moon, P. and Spencer, D. E.: Field Theory for Engineers. D. Van Nostrand, New York, 1961.

Murray, B. J., Salzmann, C. G., Heymsfield, A. J., Dobbie, S., Neely, R. R. III, Cox, C. J.: Trigonal ice crystals in Earth's atmosphere. Bulletin American Meteor. Soc. Sept. issue 1515–1531, 2015.

Nakata, M., Asano, A., Yamashita, A.: Morphology of Giant Ice Polycrystals Grown from the Vapour, Physics and Chemistry of Ice. Ed. N. Maeno and T. Hondoh, Hokkaido University Press, Sapporo, 311–317, 1992.

10 Nakaya, U.: Snow Crystals: Natural and Artificial. Harvard Univ. Press, 510 pp, 1954.

Nakaya, U., Hanajima, M., Muguruma, J.: Physical Investigations on the Growth of Snow Crystals. J. Faculty of Science, Hokkaido University. Ser. 2, 5(3), 87–118, 1958.

Nelson, J.: A Theoretical Study of Ice Crystal Growth in the Atmosphere. Ph.D. Dissertation, University of Washington, 1994.

Nelson, J.: Sublimation of Ice Crystals. J. Atmos. Sci., 55, 910–919, 1998.

15 Nelson, J.: Growth mechanisms to explain the primary and secondary habits of snow crystals. Philosophical Magazine A, 81, 2337-2373, 2001.

Nelson, J.: Branch Growth and Sidebranching in Snow Crystals. Crystal Growth & Design, 5, 1509–1525, 2005.

Nelson, J.: http://www.storyofsnow.com/blog1.php/ April 10th, 2014 post (Accessed June, 2018), 2014.

Nelson, J., and Baker, M. B.: New Theoretical Framework for Studies of Vapor Growth and Sublimation of Small Ice Crystals in the
20 Atmosphere. J. Geophys. Res. D **101**, 7033–7047, 1996.

Nelson, J., and Knight, C.: A new technique for growing crystals from the vapor. J. Cryst. Gr. 169, 795–797, 1996.

Nelson, J., and Knight, C.: Snow Crystal Habit Changes Explained by Layer Nucleation. J. Atmos. Sci., 55, 1452–1465, 1998.

Neshyba, S., Adams, J., Reed, K., Rowe, P. M., Gladich, I.: A quasi-liquid mediated continuum model of faceted ice dynamics. J. Geophys. Res., 121, 14,035–14,055, doi.org/10.1002/2016JD025458, 2016.

25 Pfalzgraff, W. C., Hulscher, R. M., and Neshyba, S. P.: Scanning electron microscopy and molecular dynamics of surfaces of growing and ablating hexagonal ice crystals. Atmos. Chem. Phys., 10, 2927–2935, 2010.

Sassen, K. and Takano, Y.: Parry arc: a polarization lidar, ray-tracing, and aircraft case study. Appl. Opt., 39, 6738–6745, 2000.

Sears, G. W.: A growth mechanism for mercury whiskers. Acta Metal., 3, 361–366, 1955.

Seligman, G.: Snow structure and ski fields: being an account of snow and ice forms met with in nature and a study on
30 avalanches & snowcraft. Macmillan & Co., Ltd. 555 pp, 1936.

Schnaiter, M., Järvinen, E., Abdelmonem, A., and Leisner, T.: PHIPS-HALO: the airborne particle habit imaging and polar scattering probe – Part 2: Characterization and first results. Atmos. Meas. Tech., 11, 341–357, 2018.

Sei, T., Gonda, T., and Goto, Y.: Formation process of branches of needle ice crystals grown from vapor. Polar Meteorol. Glaciol. 14, 27–33, 2000.

35 Shimada, W. and Ohtake, K.: Three-Dimensional Morphology of Natural Snow Crystals. Crystal Growth & Design, 16, 5603−5605, doi: 10.1021/acs.cgd.6b01263, 2016.

Shimada, W. and Ohtake, K.: Asymmetrical Three-Dimensional Morphology of Growing Snow Crystals Observed by a Michelson Interferometer. Crystal Growth & Design, 18, 6426−6430, doi: 10.1021/acs.cgd.8b01377, 2018.

Smith, H. R., Connolly, P. J., Baran, A. J., Hesse, E., Andrew R.D. Smedley, A. R. D., Webb, A. R.: Cloud chamber laboratory
40 investigations into scattering properties of hollow ice particles. J. Quant. Spectrosc. & Radiat. Transf., 157, 106–118, 2015.

Swanson, B., and Nelson, J. (in preparation).

Takahashi, C. and Mori, M.: Growth of snow crystals from frozen water droplets, Atmos. Res., 82, 385–390, doi:10.1016/j.atmosres.2005. 12.013, 2006.

Takahashi, T.: Influence of Liquid Water Content and Temperature on the Form and Growth of Branched Planar Snow Crystals in a Cloud. J. Atmos. Sci., 71, 4127–4142, 2014.

Takahashi, T., Endoh, T., Wakahama, G., and Fukuta, N.: Vapor Diffusional Growth of Free-Falling Snow Crystals between -3 and -23 °C. J. Meteorol. Soc. Japan, 69, 15–30, 1991.

Vekilov, P. G., Lin, H., and Rosenberger, F.: Unsteady crystal growth due to step-bunch cascading. Phys. Rev. E. 55, 3202–3214 doi.org/10.1103/PhysRevE.55.3202, 1997.

Voigtländer, J., Chou, C., Bieligk, H., Clauss, T., Hartmann, S., Herenz, P., Niedermeier, D., Ritter, G., Stratmann, F., and Ulanowski, Z.: Surface roughness during depositional growth and sublimation of ice crystals, Atmos. Chem. Phys., 18, 13687–13702, https://doi.org/10.5194/acp-18-13687-2018, 2018.

Westbrook, C. D.: Origin of the Parry arc. Q. J. R. Meteorol. Soc., 137, 538–543, 2011.

Wood, S. E., Baker, M. B., and Calhoun, D.: New model for the vapor growth of hexagonal ice crystals in the atmosphere, J. Geophys. Res., 106, 4845–4870, 2001.

Yamashita, A.: Skeleton Ice Crystals of Non-Hexagonal Shape Grown in Free Fall, J. Meteorol. Soc. Jpn., 49, 215–231, 1971.

Yamashita, A.: On the Trigonal Growth of Ice Crystals. J. Meteorol. Soc. Jpn., 51, 307–317, 1973.

Yamashita, A.: Small artificial snow crystals grown in free fall. J. Japanese Association of Crystal Growth, 6, 75–85, 1979. (In Japanese)

Yamashita, A.: Morphology of Plate-type Snow Crystals Grown in a Supercooled Cloud. Tenki, 60. 23–33, 2013. (In Japanese).

Yamashita, A., unpublished manuscript "Protruding Growth of Snow Crystals -Potential Role of an Adjoining-face Process", 2014.

Yamashita, A.: Adjoining Face Process and growth of Snow Crystals. JSSI&JSSE Joint Conference, Matsumoto, Japan 2015.9.13-9.16. p 24 (C1-1), 2015. (In Japanese)

Yamashita, A.: Study on Air Pockets Enclosed in Snow Crystal Part I-Air Pockets of Plate-. Tenki 63, 15–22, 2016. (In Japanese)

Yamashita, A.: unpublished manuscript "Study on comparatively large air pockets" AP Note No. 4, Nov. 2018.

Yamashita, A., Asano, A.: Morphology of Ice Crystals Grown from the Vapour at Temperatures between −4 and −1.5 °C. *J. Meteorol. Soc. Japan*, 62, 40–45, 1984.

Yamashita, A., Ohno, T.: Ice Crystals Grown in an Unforced Air Flow Cloud Chamber, J. Meteor. Soc. Jpn., 62, 135–139, 1984.